

Sponsor TBD Report No.:

**AISI/DOE Technology Roadmap Program**

**Final Report**

**QUANTIFYING THE THERMAL BEHAVIOR OF SLAGS**

**By**

**Alan W. Cramb**

**May 2003**

**Work Performed under Cooperative Agreement  
No. DE-FC36-97ID13554**

**Prepared for  
U.S. Department of Energy**

**Prepared by  
American Iron and Steel Institute  
Technology Roadmap Program Office  
Pittsburgh, PA 15222**

## **DISCLAIMER**

“Any opinions, findings, and conclusions or recommendations expressed in this material are those of the author(s) and do not necessarily reflect the views of the US Department of Energy.”

Number of pages in this report: 71

For availability of this report, contact:  
Office of Scientific and Technical Information  
P.O. Box 62  
Oak Ridge, TN 37831  
(615) 576-8401.

## **Table of Contents**

	<u>Page</u>
Table of Contents	iii
List of Figures	iv
List of Tables	ix
EXECUTIVE SUMMARY	x
1. Introduction	1
2. Major Findings and Work Completed	2
Objective 1: Develop a systematic understanding of the effect of cooling rate on slag solidification	2
Objective 2: Develop a systematic understanding of the effect of slag chemistry on slag solidification behavior	5
Objective 3: Develop a method to characterize slag melting	10
Objective 4: Develop an understanding of the role of the environment on slag solidification and melting	14
Objective 5: Develop the ability to understand slag solidification under the conditions that occur in a continuous caster	20
Objective 6: Develop an ability to predict the solidification behavior of slags	25
Objective 7: Develop the criteria for optimization of slags in steelmaking environments where they are under thermal gradients	35
3. Conclusions	49
4. Appendix 1	53

## **List of Figures**

	<b><u>Page</u></b>
Figure 1: The Double Hot Thermocouple Apparatus	2
Figure 2: Electrode Schematic	3
Figure 3: An Isothermal Experiment	3
Figure 4: A Differential Cooling Experiment	4
Figure 5: A Continuous Cooling Experiment	4
Figure 6: Phase Diagram of Calcium Aluminate	5
Figure 7: CCT Diagram for three Calcium Aluminate Slags	6
Figure 8: TTT Curve for three Calcium Aluminate Slags	6
Figure 9: Example of a CCT Curve for Mold Slag E3	7
Figure 10: Ternary Phase Diagram of CaO-MgO-Al <sub>2</sub> O <sub>3</sub>	8
Figure 11: TTT Curve for four CaO-MgO- Al <sub>2</sub> O <sub>3</sub> Slags, as indicated in Figure 10.	8
Figure 12: Critical Cooling Rate as a Function of MgO Content	9
Figure 13: TTT Curve for CS-1	9
Figure 14: Effect of Boria Addition on Slag Solidification	10
Figure 15: Melting Behavior of a Typical Slag	11
Figure 16: Crystals Breaking Apart and Moving Toward Hot Thermocouple During Melting	12
Figure 17: Temperature Profile of Melting of Industrial Mold Slag at a Low Heating Rate	13
Figure 18: Temperature Profile of Melting of Industrial Mold Slag at a High Heating Rate	14
Figure 19: Water Content in CaO-Al <sub>2</sub> O <sub>3</sub> Slags (at 1600° C) as a Function of Square Root of Water Vapor Pressure	15

## **List of Figures (Cont.)**

	<u>Page</u>
Figure 20: Crystallization Phenomena of Slag Sample at 1240° C Isothermal under Water Poor Atmosphere	15
Figure 21: Time Temperature Transformation (TTT) Curves for the Onset of Crystallization of the Sample under Ar Atmosphere and Ar + Water Vapor Atmosphere	16
Figure 22: The Relationship between Growth Velocity (V) and Isothermal Temperature (T) of the Sample from Ar and Ar+Water Vapor Conditions	17
Figure 23: Continuous Cooling Transformation (CCT) Curves for the Onset of Crystallization of the Sample under Ar Atmosphere and Ar + Water Vapor Atmosphere	17
Figure 24: Time Temperature Transformation (TTT) Curves for the Onset of Crystallization of the Sample under Moisture Atmosphere and Moisture-free Atmosphere	18
Figure 25: Continuous Cooling Transformation (CCT) Curves for the Onset of Crystallization of the Sample under Moisture Atmosphere and Moisture-free Atmosphere	19
Figure 26: The Relationship between Growth Velocity and Isothermal Temperature of the Sample from Moisture and Moisture-free Conditions	19
Figure 27: Predicted Gap Temperature for an Industrial Slab Caster	21
Figure 28: Predicted Steel Shell Temperature together with TTT Curves for E3 and STSP 816	21
Figure 29: The Onset of Crystallization for Sample E3 when run through the Temperature Time Profile of the Hot Face of the Columbus Stainless Caster	22
Figure 30: Predicted Steel Shell Temperature together with CCT Curve for Sample E3	23
Figure 31: X-ray Diffraction Pattern of STSP 816 Sample collected from the Mold	23

## **List of Figures (Cont.)**

	<u>Page</u>
Figure 32: Comparison of Measured Heat Flux of the Wideface of the Caster between Period of Steam Leaks and No Steam Leaks	24
Figure 33: The Relationship between the Growth Rate (U) and the Crystallization Time of a Eutectic CaO-Al <sub>2</sub> O <sub>3</sub> Slag at Different Temperatures	26
Figure 34: The Relationship between the Measured Growth Rate and the Calculated Nucleation Rate of a Eutectic CaO-Al <sub>2</sub> O <sub>3</sub> Slag at Different Temperatures	27
Figure 35: The Viscosity of CaO-Al <sub>2</sub> O <sub>3</sub> Slag	28
Figure 36: The Relationship between Entropy Change and Temperature of a Eutectic CaO-Al <sub>2</sub> O <sub>3</sub> Slag	29
Figure 37: The Relationship between the Nucleation Rate and Solid-Liquid Interfacial Energy of Eutectic CaO-Al <sub>2</sub> O <sub>3</sub> Slag at Different Temperatures	29
Figure 38: The Droplets of Liquid CaO-Al <sub>2</sub> O <sub>3</sub> Slag on the Surface of B-type Thermocouples at 1600° C	30
Figure 39: The Effect of Heterogeneous Nucleation on the Value of Solid-Liquid Interfacial Energy	31
Figure 40: The Effect of Heterogeneous Nucleation on TTT Curve	31
Figure 41: The Viscosity of CaO-Al <sub>2</sub> O <sub>3</sub> Slag under Dry and Humid Atmosphere	32
Figure 42: The Relationship between Growth Rate and Nucleation Time Of Eutectic CaO-Al <sub>2</sub> O <sub>3</sub> -0.042% Water Slag for Different Temperatures	32
Figure 43: The Relationship between Measured Growth Rate and Calculated Nucleation Rate of Eutectic CaO-Al <sub>2</sub> O <sub>3</sub> -0.042% Water Slag for Different Temperatures	33
Figure 44: The Effect of Humid Atmosphere on the Wettability of CaO-Al <sub>2</sub> O <sub>3</sub> Slag on the Surface of B-type Thermocouple	33

## **List of Figures (Cont.)**

	<u>Page</u>
Figure 45: The Relationship between Nucleation Rate and Solid-Liquid Interfacial Energy of Eutectic CaO-Al <sub>2</sub> O <sub>3</sub> -0.042% Water Slag for Different Temperatures	34
Figure 46: TTT Diagram for Crystallization of Experimental Mold Slag Sample E1	36
Figure 47: TTT Diagram for Crystallization of Experimental Mold Slag Sample E2	37
Figure 48: TTT Diagram for Crystallization of Experimental Mold Slag Sample E3	37
Figure 49: Comparison of the Beginning of Crystallization for Mold Slags with Different Ratios of CaO and SiO <sub>2</sub>	38
Figure 50: Comparison of the Beginning of Crystallization for Mold Slags with Different Contents of Al <sub>2</sub> O <sub>3</sub>	39
Figure 51: Comparison of the Beginning of Crystallization for Mold Slags with Different Contents of Na <sub>2</sub> O	39
Figure 52: TTT Curves showing the Effects of Na <sub>2</sub> O on the Incubation Time for the Onset of Crystallization	40
Figure 53: Schematic Representation of Morphological Layers in the Sample	41
Figure 54: Experimental Images for Different Cooling Rates of the Hot Side (Left Hand Side) taken 60s after Experiment Start. The Transparent Phase close to the Right Hand Side is Glossy, the Gray Phase is Crystalline, and the Left Side is Remaining Liquid	41
Figure 55: Crystalline Fraction as a Function of Time for Different Cooling Rates	42
Figure 56: Crystalline Fraction as a Function of Time for Different Cooling Rates	43
Figure 57: Crystalline Fraction as a Function of Time for Different Cooling Rates	43
Figure 58: TTT and CCT Curve for Beginning of Crystallization for GR-503045	

## **List of Figures (Cont.)**

		<b><u>Page</u></b>
Figure 59:	TTT and CCT Curve for Beginning of Crystallization for S-A	45
Figure 60:	TTT and CCT Curve for Beginning of Crystallization for STSP-816	46
Figure 61:	The Effect of Start Temperature for the Determination of CCT Curve for S-A	47
Figure 62:	Onset of Crystallization under both Isothermal and Continuous Cooled Experiments for M481	48
Figure 63:	Onset of Crystallization under both Isothermal and Continuous Cooled Experiments for LV 905/BC	48



## **List of Tables**

	<u>Page</u>
Table 1: Mold Slag E3	7
Table 2: Slags with Silica and Boria	10
Table 3: Composition of STSP 816 Before and After Use	22
Table 4: Composition of Experimental Mold Slags and Type of Experiment Performed	35
Table 5: Industrial Mold Slag Composition	44
Table 6: Critical Cooling Rates for Glass Formation of Industrial Mold Slags	49

## EXECUTIVE SUMMARY

This project had two goals: (1) The further development of a tool that will have broad use in the quantification of slag melting and solidification behavior, and, (2) The development of a set of meaningful design criteria for slag application in steel mill environments.

The solidification behavior of CaO-Al<sub>2</sub>O<sub>3</sub> based slags and the ternary CaO-Al<sub>2</sub>O<sub>3</sub>-MgO based slags were investigated with the double hot thermocouple technique (DHTT). Isothermal and continuous cooling experiments were employed to study these slag samples. These experiments were conducted under both dry and humid atmospheres. These slag samples were easily undercooled and the solidification behavior of CaO-Al<sub>2</sub>O<sub>3</sub> based slags was found to be a strong function of cooling rate. Then, TTT diagrams of these slag samples were created. The TTT and CCT diagrams of CaO-Al<sub>2</sub>O<sub>3</sub> based slags and TTT and CCT diagrams of ternary CaO-Al<sub>2</sub>O<sub>3</sub>-MgO based slag were generated for the first time in this work. All of the slags evaluated could form glasses at a high cooling rate and an intermediate crystalline/glass structure at moderate cooling rates.

In CaO-Al<sub>2</sub>O<sub>3</sub> based slags, the position of the TTT curve changes with the chemical composition of the slag samples and the ease of glass formation follows the trends suggested by the phase diagram. The higher the liquidus, the higher is the cooling rate necessary to form a glass. The easiest glass forming composition is the eutectic composition.

In CaO-Al<sub>2</sub>O<sub>3</sub>-MgO based slags (CaO:Al<sub>2</sub>O<sub>3</sub>≈1), the increase in MgO content also causes the position and the shape of TTT curves to change. When the MgO content increases from 0 to 3.6 % MgO, the TTT curve moves slightly upward in temperature toward lower times. After the MgO content changes from 3.6 to 7.1 % MgO, the shape of the TTT curve changes and becomes a double nose curve, where the nose at high temperature is behind the nose at low temperature. For 9 % MgO slag sample, the shape of the TTT curve is also double nose and the position of TTT curve moves slightly in front of the TTT curve of the 7.1 % MgO slag sample. Thus, the ability of a given slag to form a glass follows the liquidus surface of the phase diagram. Similar results were found when silica and boron were added.

Normally, critical cooling rate is used as the parameter for a determination of the crystallization tendency or of glass formation. A high critical cooling rate means the high crystallization tendency. The critical cooling rate of these slag samples was estimated from the position of the nose of TTT curves and this critical cooling rate was compared to the critical cooling rate obtained from CCT curves. It was found that the critical cooling rate from TTT curve is always more than the critical cooling rate from CCT curve as expected. In CaO-Al<sub>2</sub>O<sub>3</sub> based slags, the eutectic composition gives the lowest critical cooling rate due to the lowest liquidus temperature from eutectic composition. In CaO-Al<sub>2</sub>O<sub>3</sub>-MgO based slags, the critical cooling rate increases with MgO content because the high MgO content lead to the high liquidus temperature.

In this work, the effect of dissolved water on the solidification behavior of these slags was also studied. In a eutectic CaO-Al<sub>2</sub>O<sub>3</sub> slag sample, dissolved water in the sample changes the position of the TTT curve by moving the TTT to higher temperature and lower times, thus to higher critical cooling rate. The dissolved water content also enhances the growth velocity of eutectic CaO-Al<sub>2</sub>O<sub>3</sub> slag sample. Thus it can be concluded that dissolved water enhanced the crystallization tendency of this slag. It was also found that the crystalline phase that formed during cooling in both the dry and humid conditions is the mixture between 3CaO.Al<sub>2</sub>O<sub>3</sub> and CaO.Al<sub>2</sub>O<sub>3</sub> phases.

In CaO-Al<sub>2</sub>O<sub>3</sub>-MgO slag samples, in general there was little effect of water vapor in solidification behavior compared to CaO-Al<sub>2</sub>O<sub>3</sub> based slags. It was found that dissolved water hinders the crystallization behavior of 3CaO.Al<sub>2</sub>O<sub>3</sub>+3CaO.2Al<sub>2</sub>O<sub>3</sub>.MgO, which formed at high temperature and had no effect on crystallization of 3CaO.Al<sub>2</sub>O<sub>3</sub>+MgO.Al<sub>2</sub>O<sub>3</sub>, which formed at low temperature. The effect of dissolved water on the crystallization of CaO-Al<sub>2</sub>O<sub>3</sub>-MgO based slags is not as prominent as in the eutectic CaO-Al<sub>2</sub>O<sub>3</sub> slag. Thus, the addition of MgO to CaO-Al<sub>2</sub>O<sub>3</sub> slags was seen to minimize or eliminate the effect of humidity on the solidification of CaO-Al<sub>2</sub>O<sub>3</sub> based slags. This is also a novel and major finding of this work.

The growth velocity of CaO-Al<sub>2</sub>O<sub>3</sub> based slags and of ternary CaO-Al<sub>2</sub>O<sub>3</sub>-MgO based slags were measured for the first time. In CaO-Al<sub>2</sub>O<sub>3</sub> based slags, the growth velocity was in the range between 5 to 350 μm/sec. depending on temperature and composition of the slag samples. At a given isothermal temperature, the eutectic CaO-Al<sub>2</sub>O<sub>3</sub> slag sample gave the slowest growth velocity. In all slag samples, increased isothermal temperature enhanced diffusion rate and resulted in a higher growth velocity. Dissolved water in the eutectic CaO-Al<sub>2</sub>O<sub>3</sub> slag sample decreased the viscosity of the slags by breaking tetrahedral network in the structure of liquid slags due to segregation during solidification and this resulted in a higher local growth velocity. In CaO-Al<sub>2</sub>O<sub>3</sub>-MgO based slags, for isothermal temperatures below 1200°C, the growth velocity of all CaO-Al<sub>2</sub>O<sub>3</sub>-MgO slag samples increased with increasing isothermal temperature and MgO content. For isothermal temperatures above 1200°C, the growth velocity decreased. This occurred because the growth velocity was retarded by the formation of the new phase from the second nose of the TTT curve. Dissolved water enhanced the growth velocity when isothermal temperature was lower than 1170°C and hindered the growth velocity when isothermal temperature is higher than 1170°C.

Uhlmann's method was used to estimate the solid-liquid interfacial energy of CaO-Al<sub>2</sub>O<sub>3</sub> based slag for the temperature between 1100°-1250°C. The results are shown in the following equations:

by assuming heterogeneous nucleation (40° contact angle)

$$g_{sl}(J/m^2) = 1.1893 - 0.0007 \cdot T(C)$$

Dissolved water in CaO-Al<sub>2</sub>O<sub>3</sub> based slag also increases the solid-liquid interfacial energy. And this work allows a prediction of the solid-liquid interfacial energy in presence of water:

$$g_{sl}(J/m^2) = 2.1473 - 0.0012 \cdot T(C)$$

It appears that water vapor affects solidification behavior in 2 ways: (1) It increases diffusion rate in the liquid ahead of growing interface due to segregation, and (2) It

changes the solid-liquid interfacial energy of the precipitating solid. Both of these effects result in a significant change to the TTT curve. However, this also leads to our ability to predict TTT and CCT curves from knowledge of diffusivity and thermodynamics.

A significant amount of work was also carried out to determine the solidification behavior of actual mold slags with similar results to those already discussed; however, high fluorine contents in a number of fluxes made the results less clear.

This project has lead to the further development of a new tool for measuring slag solidification under a wide variety of thermal conditions and also to an improved understanding of solidification behavior in that most ubiquitous of steelmaking materials – a slag. The true nature of solidification of slags has been revealed and new scientifically based criteria have been developed for understanding slag behavior: the TTT and CCT curves, the critical cooling rate for glass formation, the effect of cooling rate on solidification morphology. Thus, both deliverables of the project have been satisfied.

# **Quantifying the Thermal Behavior of Slags**

## **Final Project Report**

### **1. Introduction**

Successful operation of a continuous caster is based upon control of heat transfer in the mold. The mold slag is a key component in the success of continuous casting; however, the phenomena that occur in the gap between the shell and the mold are largely unknown as until recently there have been no techniques that allowed visualization and quantification of the solidification behavior of liquid slags. This has lead to slag design being an empirical science or art.

Recently a new experimental technique, called Double Hot Thermocouple Technique (DHTT), was developed at Carnegie Mellon University that allowed the solidification behavior of a slag to be observed and quantified under conditions that simulate the thermal conditions that occur in steelmaking environments. This technique allows ladle, tundish and mold slags to be characterized under extreme conditions including those found between the mold wall and the growing shell of a continuous caster.

Thus, a program is initiated, under this grant, to quantify and describe the phenomena that occur during the solidification of a slag in a steel mill environment. This will allow slag design to become an engineering science rather than an empirical exercise.

The project deliverables were as follows:

- The further development of a tool that will have broad use in the quantification of slag melting and solidification behavior
- The development of a set of meaningful design criteria for slag application in steel mill environments.

The project was broken down into a number of objectives:

- Develop a systematic understanding of the effect of cooling rate on slag solidification
- Develop a systematic understanding on the effect of slag chemistry changes on slag solidification behavior.
- Develop a method to characterize slag melting
- Develop an understanding of the role of the environment on slag solidification and melting
- Develop the ability to understand slag solidification under the conditions that occur in a continuous caster
- Develop an ability to predict the solidification behavior of slags
- Develop the criteria for optimization of slags in steelmaking environments where they are under thermal gradients

The purpose of this final report is to document the work that was done to achieve the above deliverables.

## **2. Major Findings and Work Completed**

### **Objective 1: Develop a systematic understanding of the effect of cooling rate on slag solidification**

The DHTT technique was further developed and fine tuned to allow slag solidification to be determined under conditions of constant temperature, a controlled cooling rate where both thermocouples were cooled at the same rate and under controlled cooling rates, where both thermocouples were cooled at different rates. This last technique allows the continuous caster gap to be simulated by allowing the potential cooling rates from thermal models of the mold to be input to the double hot thermocouple device. Details of the double hot thermocouple technique are given in Appendix 1.

The apparatus is shown in Figure 1.

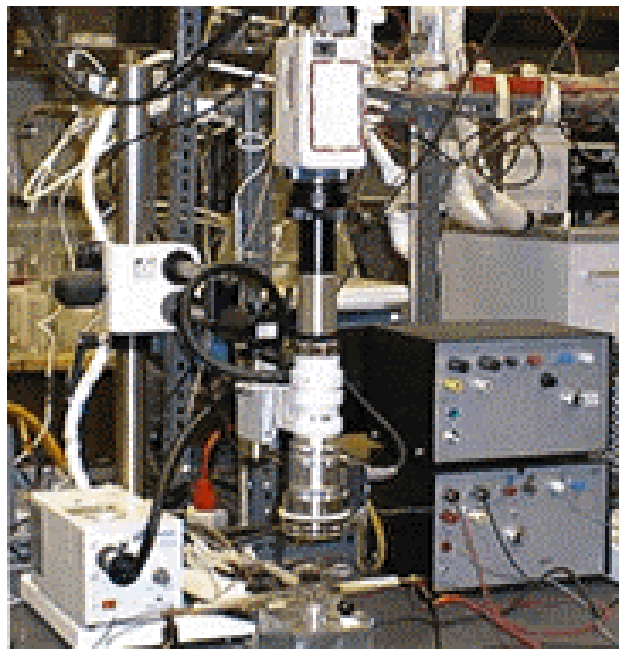


**Figure 1: The Double Hot Thermocouple Apparatus**

An illustration of the electrode structure and technique is given in Figure 2.

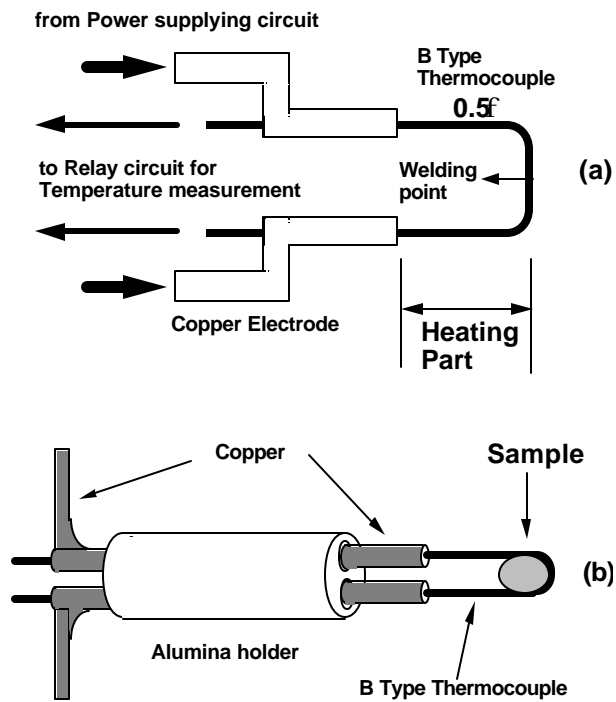


**Figure 2: Electrode Schematic**

Three possible temperature profiles are given in Figure 3, 4 and 5.

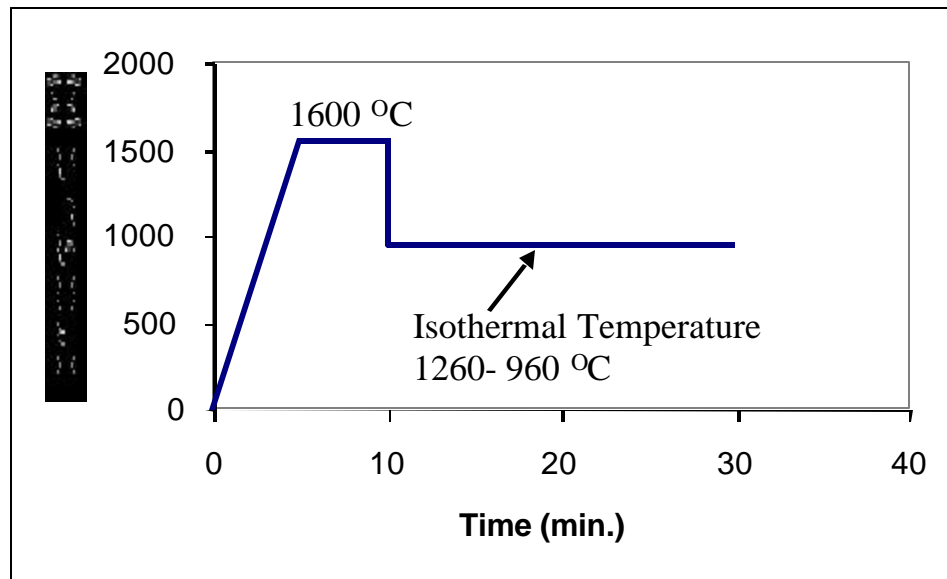


**Figure 3: An Isothermal Experiment**

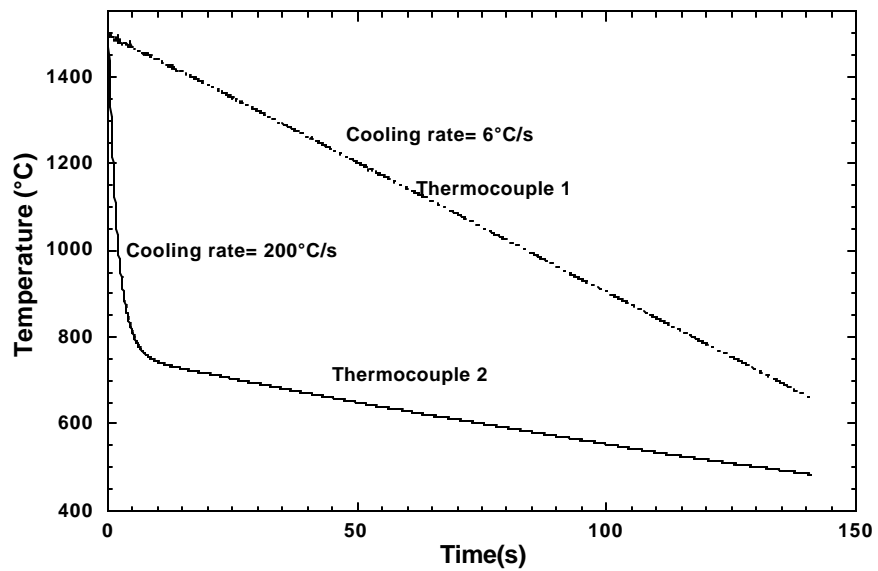


**Figure 4: A Differential Cooling Experiment**

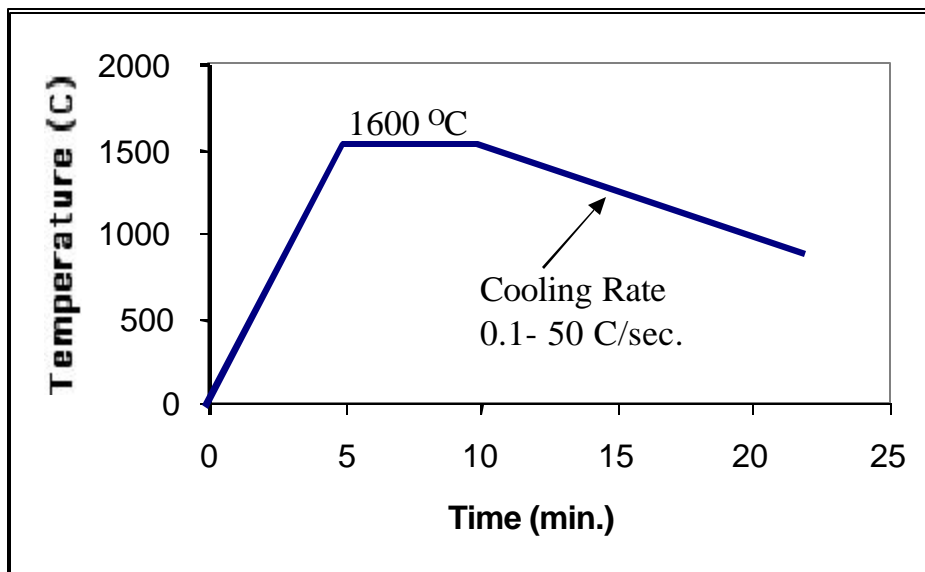


**Figure 5: A Continuous Cooling Experiment**

These techniques allow a systematic study of the cooling of a slag.



**Objective 2: Develop a systematic understanding of the effect of slag chemistry changes on slag solidification behavior.**

Under this objective the solidification behavior of  $\text{CaO-Al}_2\text{O}_3$ ,  $\text{CaO-Al}_2\text{O}_3\text{-MgO}$ ,  $\text{CaO-Al}_2\text{O}_3\text{-SiO}_2$  slags were measured in detail. The effect of sodium oxide on more complex slag chemistries was also measured. In addition, an actual mold slag was also measured. The technique is widely applicable to all but very volatile slags containing high levels of fluorine or slags containing high levels of  $\text{FeO}$  and  $\text{MnO}$ . However, as such slag formulations will be minimized in the future due to environmental or contaminant problems, this is not a major issue.

The phase diagram for calcium aluminate slags is shown in Figure 6. An example of a CCT curve for three of  $\text{CaO-Al}_2\text{O}_3$  slags noted in Figure 6 are given in Figure 7, where it can be seen that glass formation is possible in all slag formulations and that it is easiest at the eutectic composition. In this Figure it can be seen that the glass-forming tendency follows the trends of the phase diagram in these oxides.

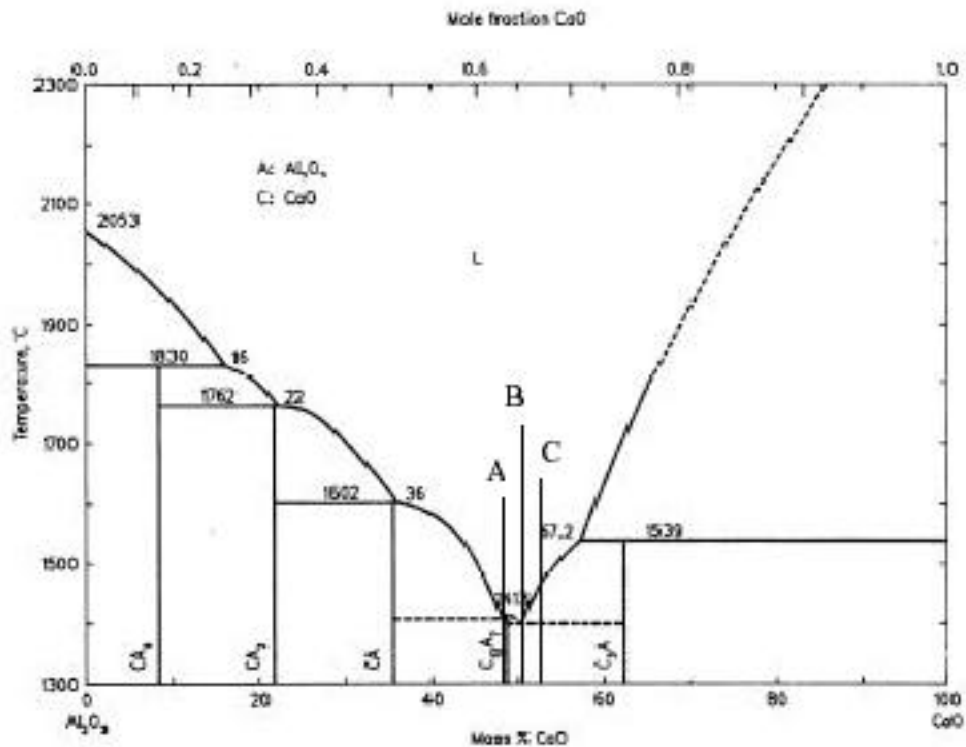


**Figure 6: Phase Diagram of Calcium Aluminate**

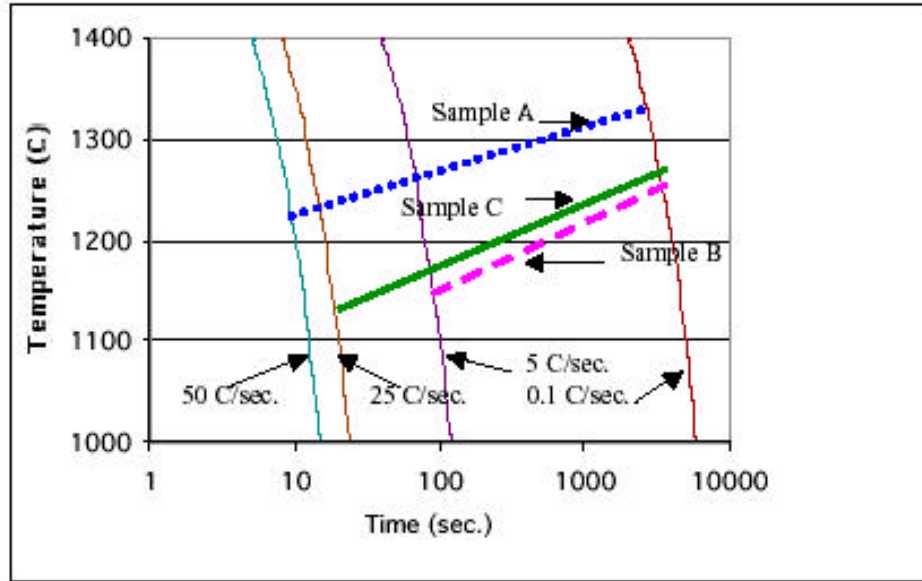


**Figure 7: CCT Diagram for three Calcium Aluminate Slags**

The TTT curve for all three slags is given in Figure 8.

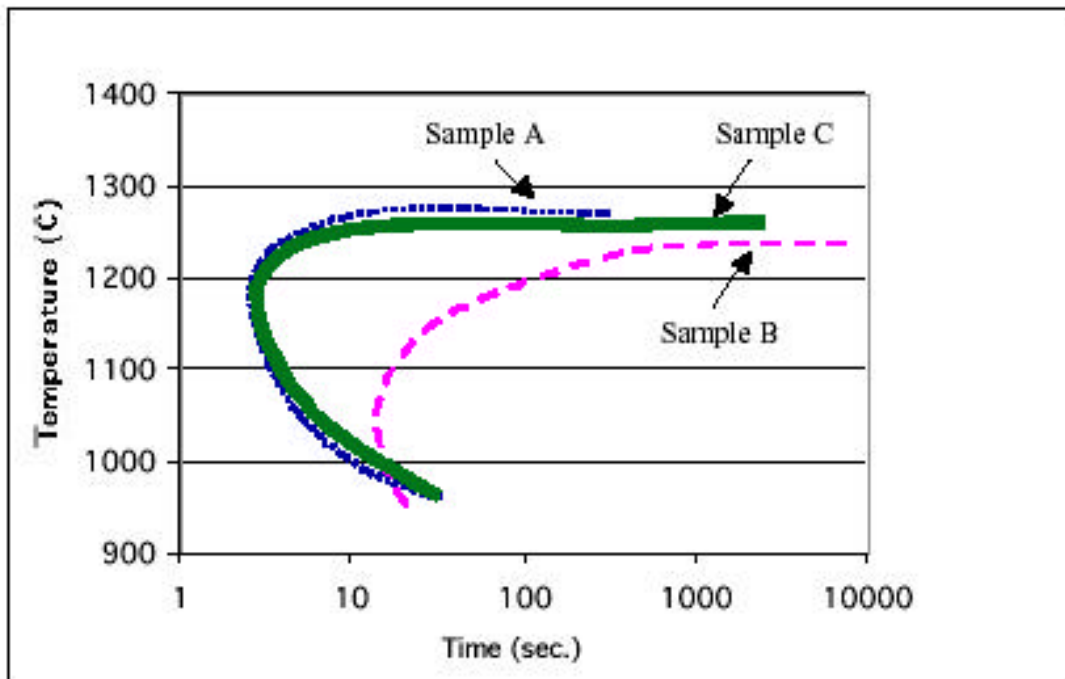


**Figure 8: TTT Curve for three Calcium Aluminate Slags**

The above TTT and CCT curves are the first such diagrams that have been developed for calcium aluminate based slags. More details are given in Appendix 1.

Similar diagrams have also been developed for mold slags. An example chemistry is given in Table 1 and an example of a CCT curve is given in Figure 9.

**Table 1: Mold Slag E3**

Sample E3				
%CaO	%SiO <sub>2</sub>	%Al <sub>2</sub> O <sub>3</sub>	%Na <sub>2</sub> O	%CaF <sub>2</sub>
39.58	40.94	6.94	9.57	1.00

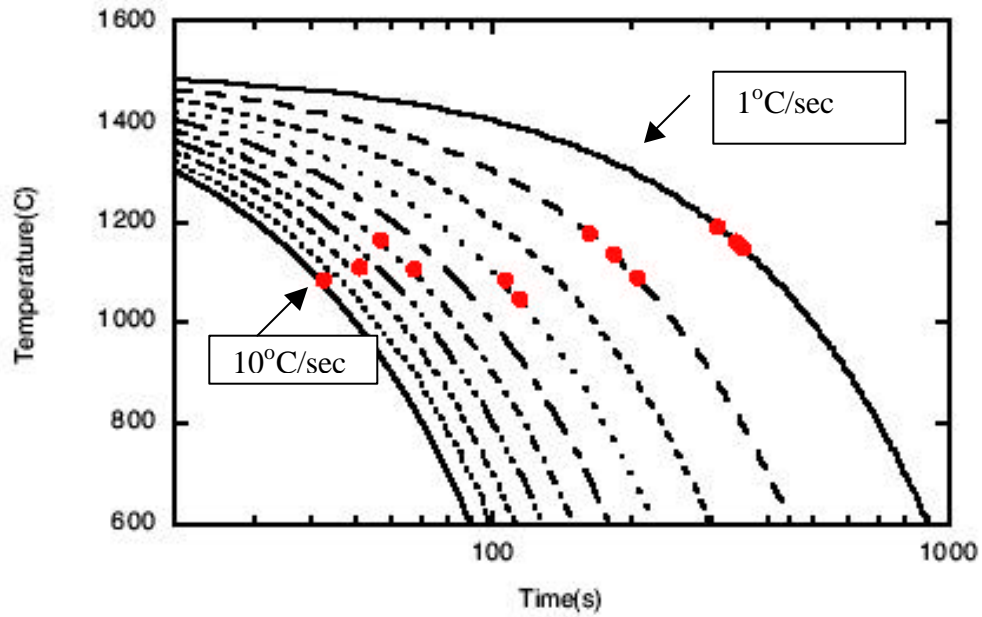


**Figure 9: Example of a CCT Curve for Mold Slag E3.**

In addition to binary slags, ternary slags in the CaO-MgO-Al<sub>2</sub>O<sub>3</sub> system were also measured. Such slags are represented in the following phase diagram (Figure 10).

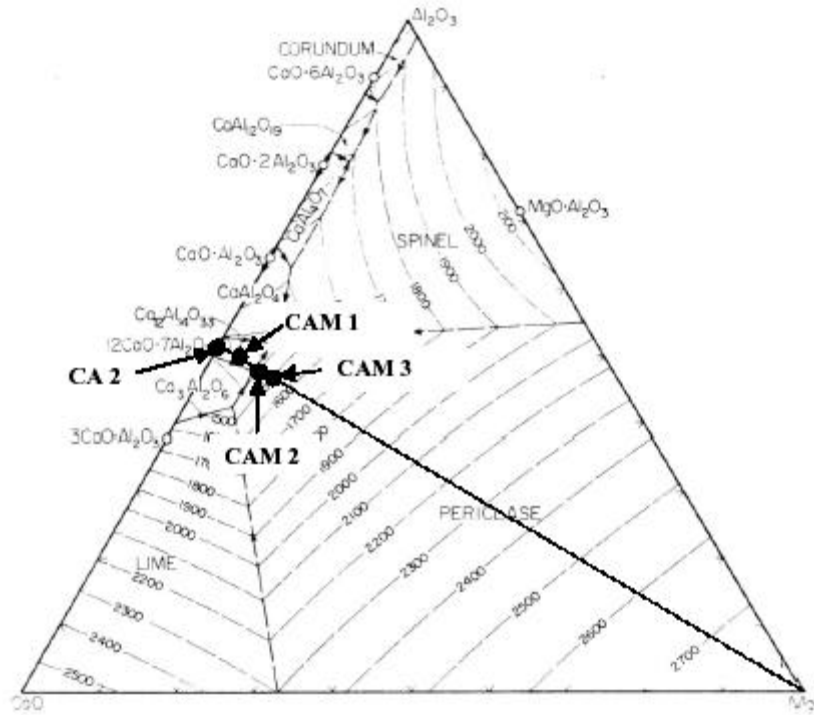


**Figure 10: Ternary Phase Diagram of CaO-MgO-Al<sub>2</sub>O<sub>3</sub>**

The results of solidification experiments are as follows (Figure 11):

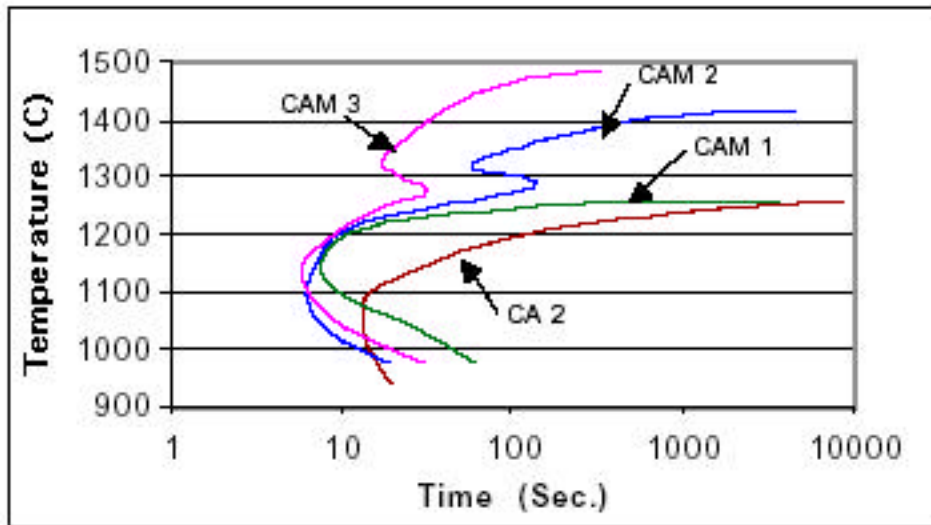


**Figure 11: TTT Curve for four CaO-MgO-Al<sub>2</sub>O<sub>3</sub> Slags, as indicated in Figure 10.**

The effect of MgO on the critical cooling rate follows the phase diagram and is shown in Figure 12, where the addition of MgO to calcium aluminate makes the slags more difficult to form as glasses.

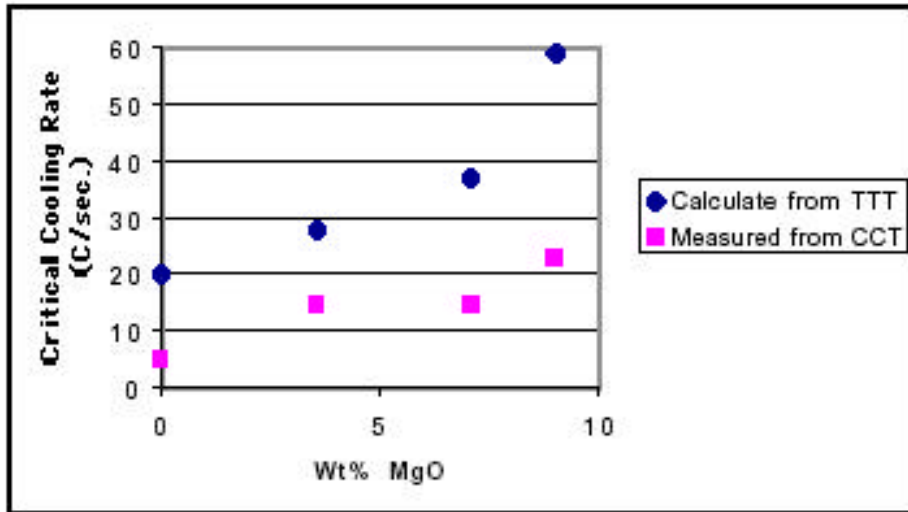


**Figure 12: Critical Cooling Rate as a Function of MgO Content**

The effect of up to 10% silica additions to eutectic calcium aluminate was also found to increase the critical cooling rate for glass formation; however, for off eutectic compositions the critical cooling rate could decrease (Figure 13).

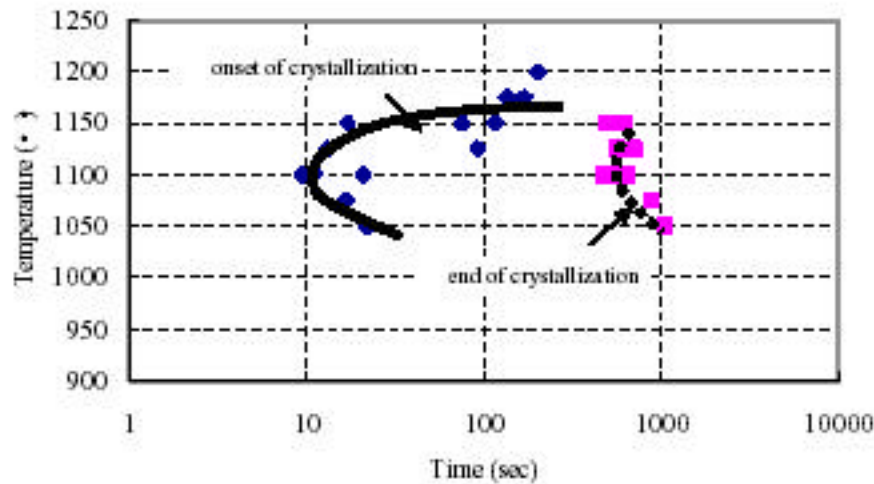


**Figure 13: TTT Curve for CS-1**

Recently there has been an interest in boria additions to slags as a replacement for  $\text{CaF}_2$ . In Table 2, two slag compositions containing silica and boria are shown.

**Table 2: Slags with Silica and Boria**

No.	CaO	Al <sub>2</sub> O <sub>3</sub>	SiO <sub>2</sub>	B <sub>2</sub> O <sub>3</sub>
CS-1	50	43	7	0
CS-2	47	41	7	5

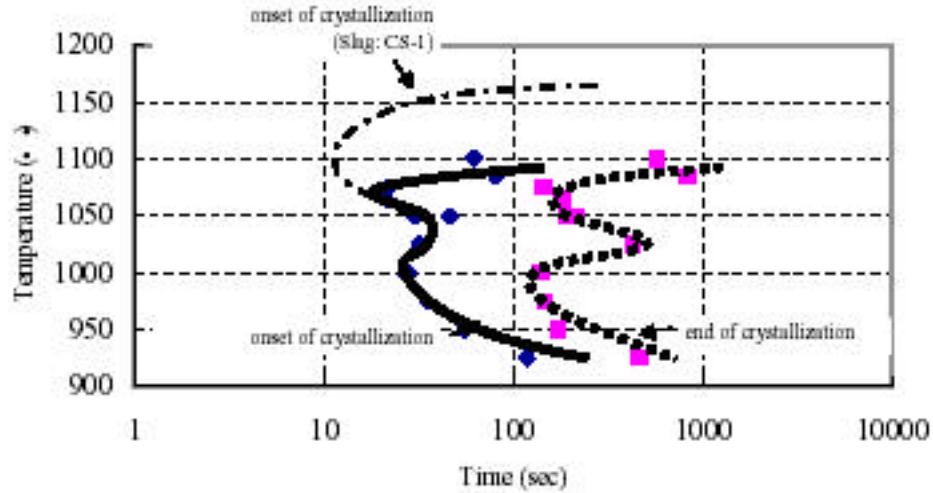


**Figure 14: Effect of Boria Addition on Slag Solidification**

In Figure 14, the effect of boria addition on the TTT curve can be seen, where boria reduces the maximum temperature of crystallization by 100° C and increase the potential for glass formation. In addition a double nose phenomenon was noted.

The above examples indicate that the technique can be used to determine the effect of chemistry on slag solidification.

### **Objective 3: Develop a method to characterize slag melting**

In a manner similar to slag solidification, slag melting can be observed as a function of heating rate.

An example of progressive melting behavior is shown in Figure 15.

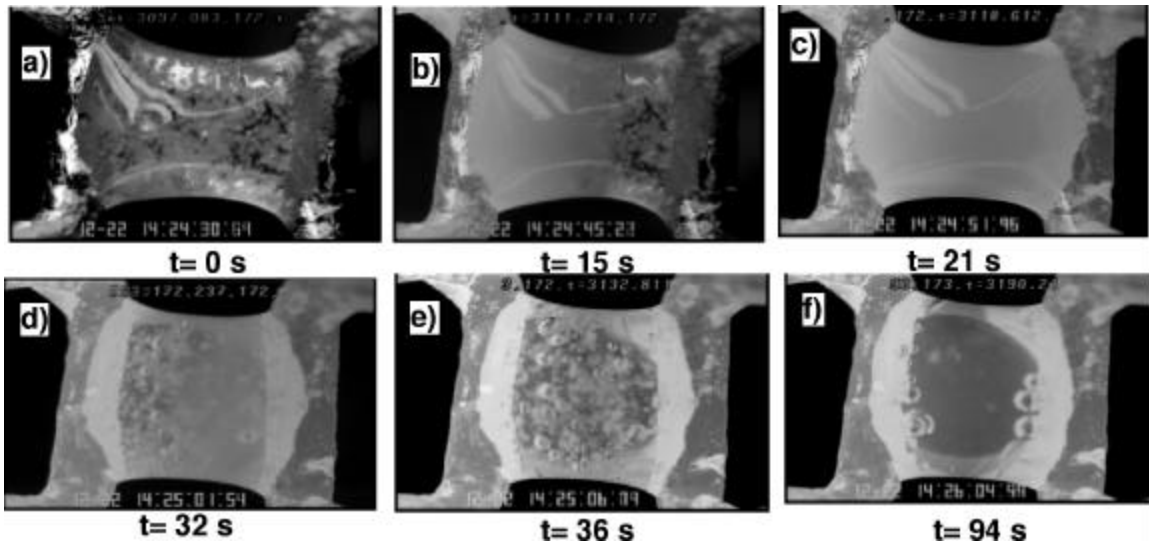


**Figure 15: Melting Behavior of a Typical Slag**

The solid sample consists, before melting, of a glassy and a light gray crystalline phase {Figure 15 (a)}. The heating starts at the left thermocouple, and the crystals already present start to grow towards the right side, with the higher crystal fraction portion of the film becoming opaque {Figure 15 (b)}.

A part of the crystalline fraction also consists of crystals that grew from nuclei that were not resolvable before the heating cycle. With increasing time, only the crystalline phase can be observed, and the sample becomes opaque {Figure 15 (c)}. As the temperature reaches the liquidus, it can be seen that the crystals start to dissolve at the left side of the sample, and the dissolution of the crystals is relatively fast {Figure 15 (d)}. With increasing time, the sample becomes transparent and many bubbles are observed {Figure 15 (e)}. The sample becomes transparent at around 1330°C. Bubbles may originate from carbonate and hydrate contamination in the powders used to mix the samples. It was also observed that the bubble formation rate was higher in samples that had been exposed to air. This indicates that moisture in the sample could also form bubbles. Bubble formation during melting was only observed at the first melting of the mold slag sample. The rate of movement of the bubbles in the mold slag sample was high due to the low viscosity of the slag at high temperature (1400°C). Eventually only a few bubbles remained stuck to the thermocouples {Figure 15 (f)}.

Both Marangoni flow and natural convection cause the movement of the bubbles. Small bubbles (<10 μm) caught in a vortex or a specific flow pattern can stay in the slag up to a minute before escaping. These observations indicate that if similar turbulent flow exists in the liquid slag pool in the actual mold, bubbles caught in the slag layer may be subsequently drawn between the mold wall and the steel strand. It is clear that, if this phenomenon occurs in an actual caster, then the presence of bubbles in the slag film will have a strong effect on the in-mold heat transfer rate. It could be argued that this would be beneficial or deleterious depending upon the requirements of the slag film in the caster. Another interesting phenomenon that was documented was the manner by which a crystallized slag melts. Under a constant heating rate, the intercrystalline glass melts first,

and the crystalline particles start to break apart from each other. Natural convection or Marangoni flows cause crystalline particles to be transported to the heating source (hot thermocouple), and subsequently melted. The major part of the crystalline fraction is melted at the heating source and not at their original position by this mechanism. Figure 16 shows crystals breaking apart, and moving toward the hot thermocouple during melting. Normally, Marangoni flows develop from hot to cold due to the gradients in surface tension caused by the thermal conditions. In these experiments, the movement that is documented is internal and not a surface flow. Therefore, it is thought that there is a strong surface flow from the thermocouple to the slag due to surface tension gradients, and a return flow (for continuity) that accounts for the movement of the solid material from the colder areas to the hotter areas. This observed melting phenomena indicates that, in slags, melting characteristics will be determined by the fraction of solid, and the details of the chemistry of the segregated liquid between the crystallized fraction. Thus, there is no specific melting temperature rather a melting range, and melting will begin as soon the interdendritic liquid reaches a temperature where its viscosity is such that fluid flow will initiate. Thus, melting phenomena will vary with heating rate, and the onset of fluid flow. The onset of melting should initiate at the dynamic solidus of the flux and end at the liquidus temperature. This effect is also seen when one has strong fluid flow across a dendritic array. For example, in melting, this crystal fragmentation leads to mass transfer from the solid phase to the hottest temperature in the system and enhanced melting rates.

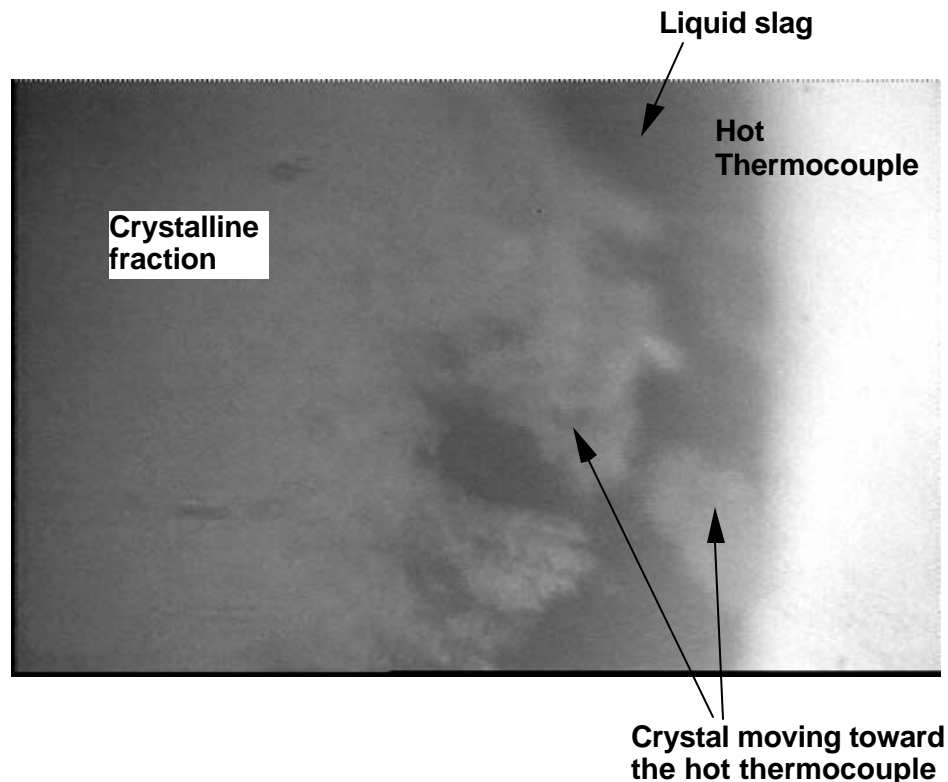


**Figure 16: Crystals Breaking Apart and Moving toward Hot Thermocouple during Melting**

The melting of an industrial mold powder/slag was investigated at different heating rates. The sample was heated at a rate of 0.64°C/s and 14.1°C/s. The start and end of the



melting were determined by direct observation using single hot thermocouple technique (SHTT). The beginning of melting was determined when liquid phase could be seen, and the end of melting, when no solid phases could be observed. The temperature profile was recorded on the computer. Figures 17 and 18 show the beginning and end of melting at low and high heating rates.

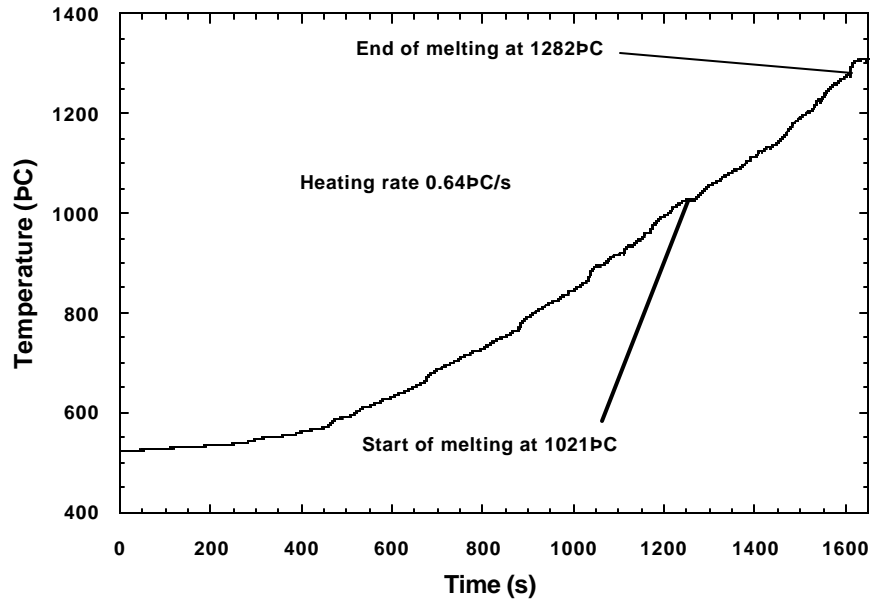


**Figure 17: Temperature Profile of Melting of Industrial Mold Slag at a Low Heating Rate.**

Bubble formation could be observed in all experiments during the melting. The bubbles formed more vigorously at the high heating rate, stirring the melt, and therefore, increasing the melting rate. It is clear from the above experiments that melting phenomena in slags are quite complex, and a function of heat flux and fluid flow conditions that are found locally in the sample. Although no attempt has been made to determine the source of bubbles, it is likely that they are associated with the decomposition of carbonates and hydrates present in the powders before melting. For the experimental mold slags containing no fluorine, vaporized fluoride species cannot be the source of the bubbles. It is also highly unlikely that rate of fluoride vaporization, in the case of fluorine containing samples, would be high enough to account for this excessive bubble formation. However, all samples contain both CaO and Na<sub>2</sub>O, two substances that easily pick up both carbon dioxide and moisture when exposed to the atmosphere. The dehydration of the samples and decomposition of hydrates and carbonates, forming H<sub>2</sub>O (g) and CO (g) respectively, during the heating up, and subsequently melting would explain the excessive amount of bubbles in the slag samples. In the current study, it was observed that the amount of bubbles increased for samples exposed for longer times to the atmosphere.

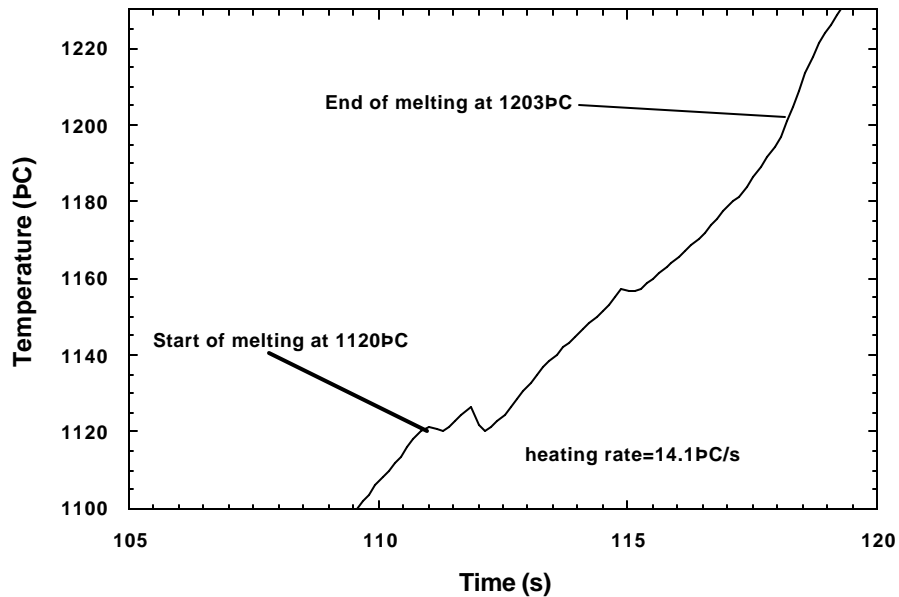


**Figure 18: Temperature Profile of Melting of Industrial Mold Slag at a High Heating Rate.**

Thus this technique is a good technique for studying the melting behavior of prefused fluxes.

#### **Objective 4: Develop an understanding of the role of the environment on slag solidification and melting**

The most obvious environmental effect is that of water vapor in the atmosphere. In general humidity increases the crystal growth rate and makes the slags solidify at a higher cooling rate making the slags harder to form as a glass.

In order to study the effect of water vapor on crystallization, experiments were conducted in two different kind of atmospheres: an Ar atmosphere and an Ar +water vapor atmosphere. The Ar -water vapor mixture was prepared by passing Ar gas at 150 ml/min through a water column, whose temperature was fixed and controlled by the condenser. The experimental partial pressure of water vapor were 0.031, 0.042 and 0.054 atm, which are equivalent to full humidity at 25°, 30° and 35°C, respectively. From the work by Schwerdtfeger and Schubert , the solubility of water vapor in CaO-Al<sub>2</sub>O<sub>3</sub> slag at 1600°C was measured with the mogravimetric method and the result is shown in Figure 19.

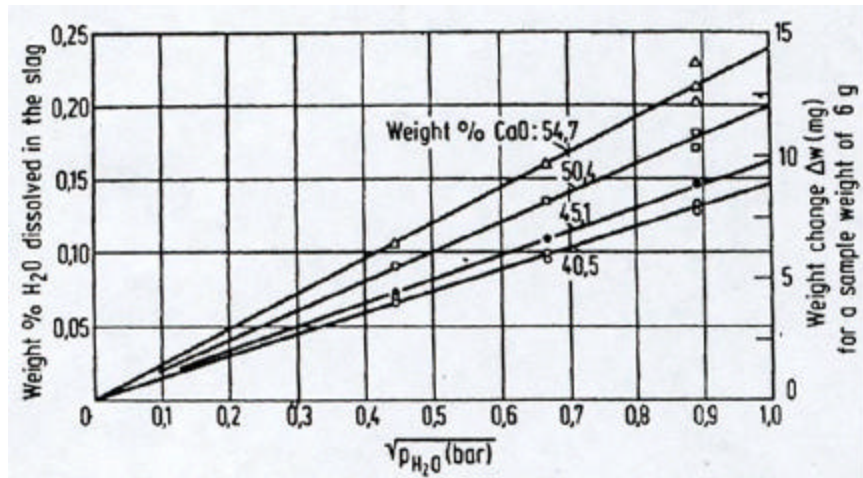


**Figure 19: Water Content in CaO-Al<sub>2</sub>O<sub>3</sub> Slags (at 1600°C) as a Function of Square Root of Water Vapor Pressure.**

An example of crystallization phenomena of the sample at 1240°C under a water vapor atmosphere is shown in Figure 20. Figure 20 shows that a nucleus precipitates at the tip of thermocouple and grows as a plane front to the tip of another thermocouple. During the growth process, 2-3 gas bubbles precipitate in front of the plane front and move along with the plane front. The gas bubbles should be H<sub>2</sub>O gas because the water dissolved in the liquid slag sample is released as a gas due to the decrease in solubility of water in the slag with temperature and segregation as the crystalline phase of the precipitated solid has no water in its chemical composition.

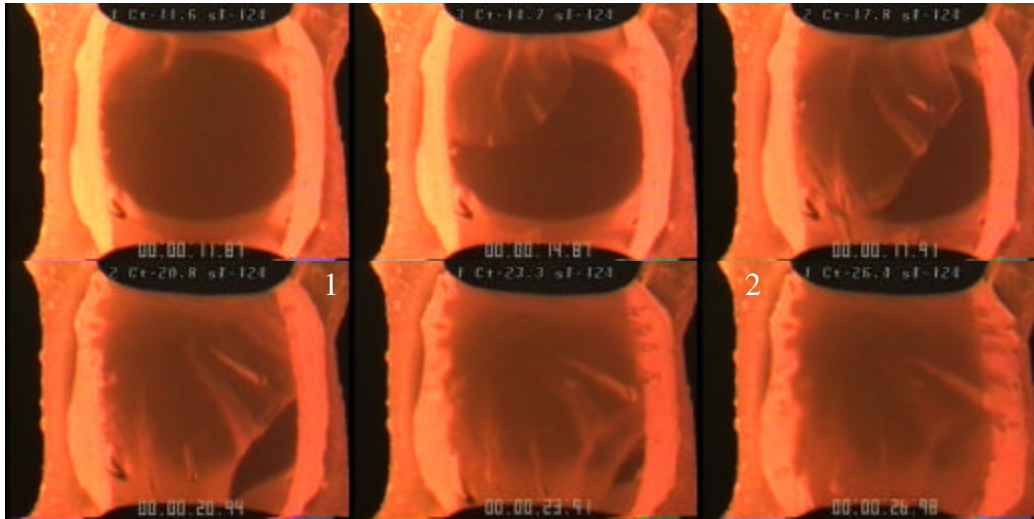


**Figure 20: Crystallization Phenomena of Slag sample at 1240°C Isothermal under Water Poor Atmosphere**

From the isothermal experiments, the TTT diagram can be created from crystallization time and crystallization temperature, as shown in Figure 21.

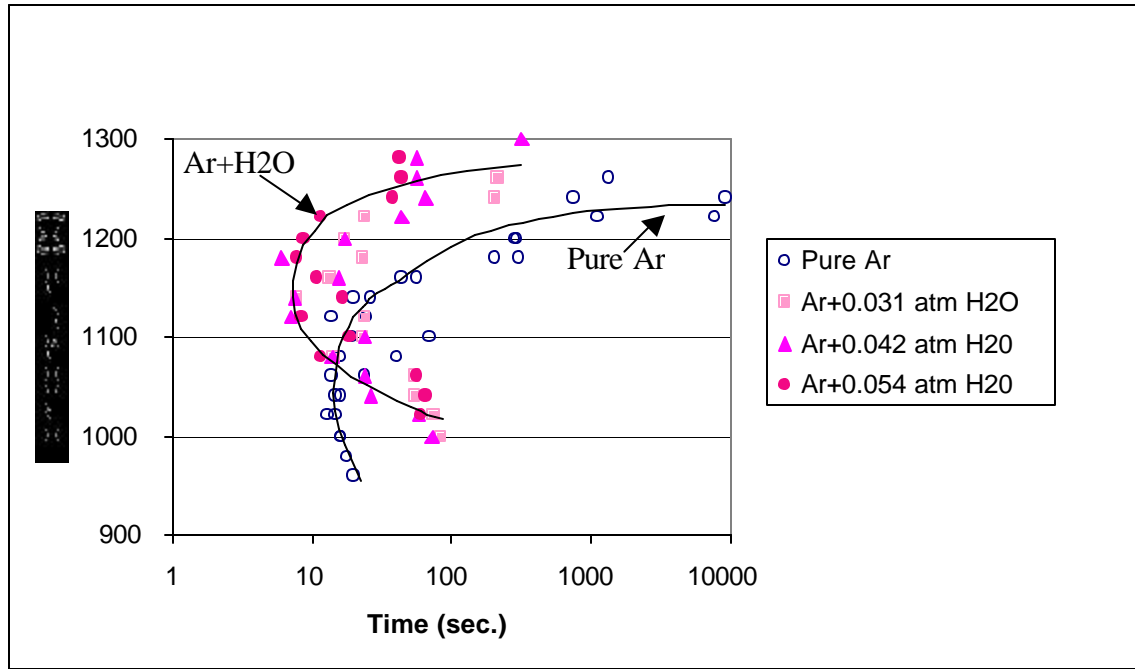


**Figure 21: Time Temperature Transformation (TTT) Curves for the Onset of Crystallization of the Sample under Ar Atmosphere and Ar + Water Vapor Atmosphere.**

The variation in the water vapor atmosphere between 0.031-0.054 atm didn't show a significant difference in the position of TTT curve as the change of the content of the water dissolved in the sample is a very small change (0.032-0.042 wt%) for the variation of the water vapor between 0.031-0.052 atm (Figure 21).

A comparison of the TTT curve from Ar and Ar + water vapor atmospheres shows that TTT curve from Ar + water vapor condition is above and in front of the TTT curve from pure Ar condition. It can be concluded that the water dissolved in slag enhanced nucleation phenomena.

In the isothermal experiments, the growth velocity can be measured under constant temperature conditions by assuming a constant growth velocity. Figure 22 shows the relationship between growth velocity and isothermal temperature of the sample from Ar and Ar + water vapor conditions.

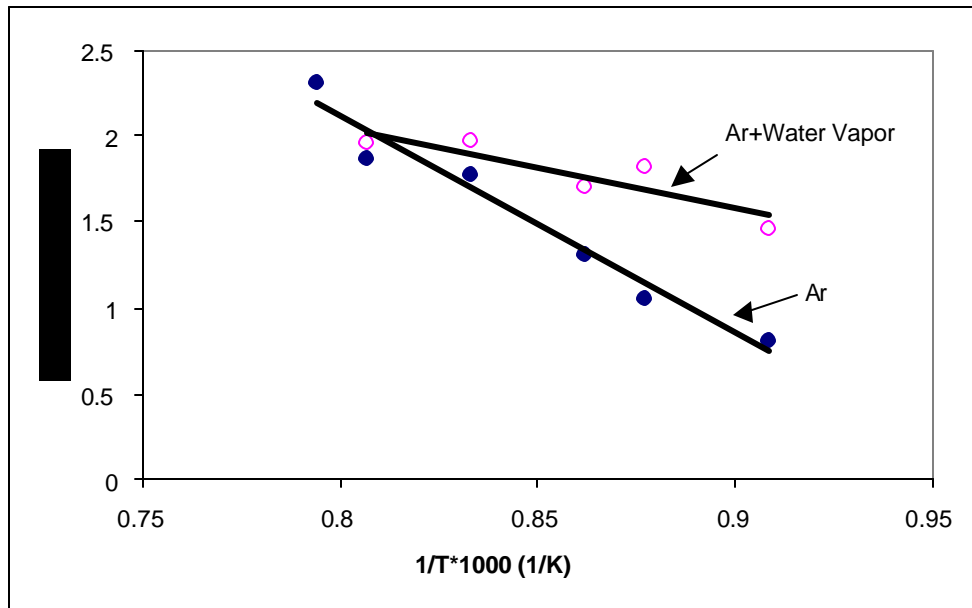


**Figure 22: The Relationship between Growth Velocity (V) and Isothermal Temperature (T) of the Sample from Ar and Ar + water Vapor Conditions.**

The growth velocity increased with increasing isothermal temperature (Figure 22). So, growth in both conditions is probably controlled by diffusion. The growth rate from slags in a humid atmosphere is higher than growth rate from dry atmospheres. However, in humid conditions the gradient of growth rate change with temperature is less than that from dry conditions. Consequently, it can be concluded that water vapor enhances the growth process. From the continuous cooling experiments, the CCT diagram can be created from crystallization time and crystallization temperature, as shown in Figure 23.

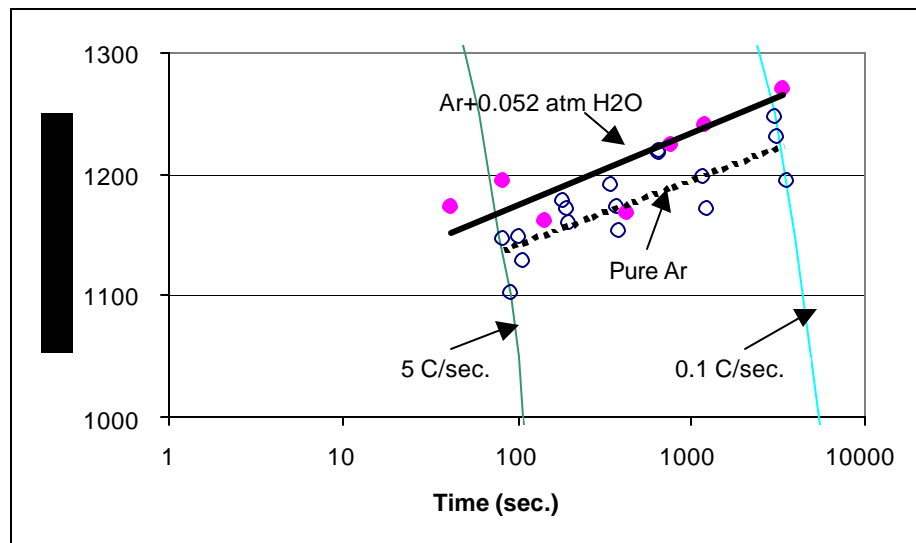


**Figure 23: Continuous Cooling Transformation (CCT) Curves for the Onset of Crystallization of the Sample under Ar Atmosphere and Ar + Water Vapor Atmosphere.**

From Figure 23, the CCT curve from water vapor condition is higher than the CCT curve from without water vapor condition by approximately 30-50°C. Then, at the same cooling rate crystallization in humid atmospheres occurs at a higher temperature and before the crystallization in dry conditions. Furthermore, the critical cooling rate in water vapor condition (10°C/sec.) is twice of the critical cooling rate in dry atmospheres (5°C/sec.).

Quite different results were discovered when studying slags containing MgO. From the isothermal experiments, the TTT diagram was created from crystallization time and crystallization temperature, as shown in Figure 24. From Figure 24, TTT curves from moisture atmosphere have a double nose, which is same as TTT curve from the moisture free atmosphere. The effect of a moist atmosphere on CaO-Al<sub>2</sub>O<sub>3</sub>-MgO slag is not as prominent as in CaO-Al<sub>2</sub>O<sub>3</sub> slag and the variation in water content does not clearly affect the TTT curve. For the nose of TTT curves at low isothermal temperature, TTT curves from moisture condition is in front of the TTT curve from moisture free condition, only when isothermal temperature is below 1100°C. However, if isothermal temperature is between 1100°-1250°C, TTT curves from both moisture and moisture-free conditions are the same. For the nose of TTT curves at high temperature, the TTT curves from moisture condition are behind TTT curve from moisture free condition. Therefore, it can be concluded that water enhanced crystallization of a CaO-Al<sub>2</sub>O<sub>3</sub>-MgO slag when isothermal temperature is lower than 1100°C. Water has no effect on crystallization of CaO-Al<sub>2</sub>O<sub>3</sub>-MgO slag, when isothermal is between 1100°-1250°C. For isothermal temperature above 1250°C, water hinders crystallization of CaO-Al<sub>2</sub>O<sub>3</sub>-MgO slag. However, these effects are small and to a first approximation water had no effect in the crystallization phenomena of the slag.

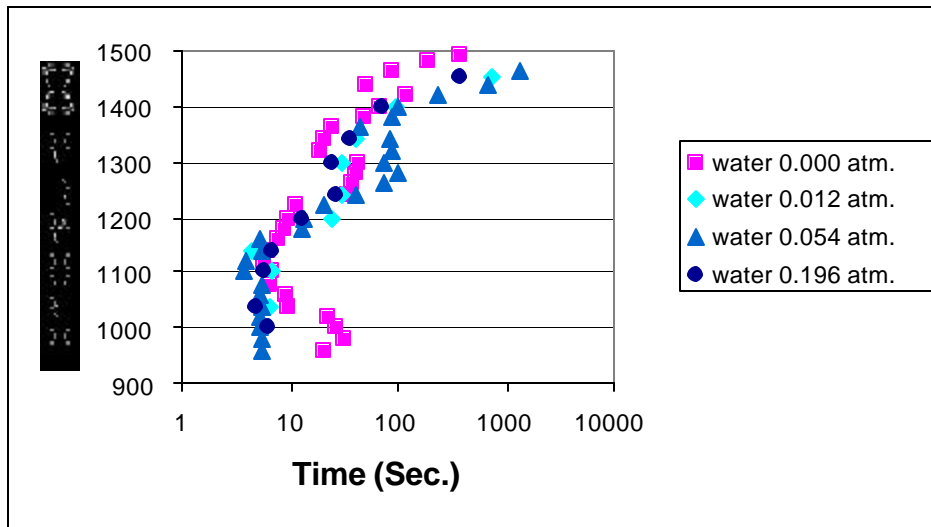


**Figure 24: Time Temperature Transformation (TTT) Curves for the Onset of Crystallization of the Sample under Moisture atmosphere and Moisture-free Atmosphere.**

From the continuous cooling experiments, the CCT diagram can be created from crystallization time and crystallization temperature, as shown in Figure 25.

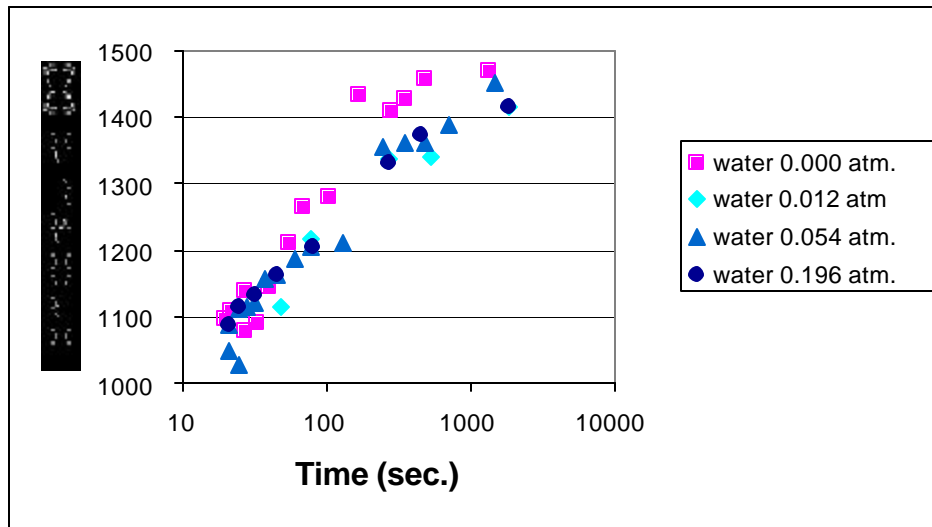


**Figure 25: Continuous Cooling Transformation (CCT) Curves for the Onset of Crystallization of the Sample under Moisture and Moisture-free Atmosphere.**

From Figure 25, at the lower part of CCT curves (cooling rate more than  $7^{\circ}\text{C}/\text{sec.}$ ), moisture has no effect on crystallization time and temperature. For the top part of CCT curves (cooling rate less than or equal to  $7^{\circ}\text{C}/\text{sec.}$ ), crystallization under moisture free conditions start at a higher temperature and shorter time than crystallization under moisture conditions. Therefore, water hinders crystallization of  $\text{CaO-Al}_2\text{O}_3\text{-MgO}$  slag when cooling rate is less than or equal to  $7^{\circ}\text{C}/\text{sec.}$  In addition, water did not affect the critical cooling rate. If the effect of water on TTT and CCT is compared, it was found that water hinders crystallization at the high temperature only.

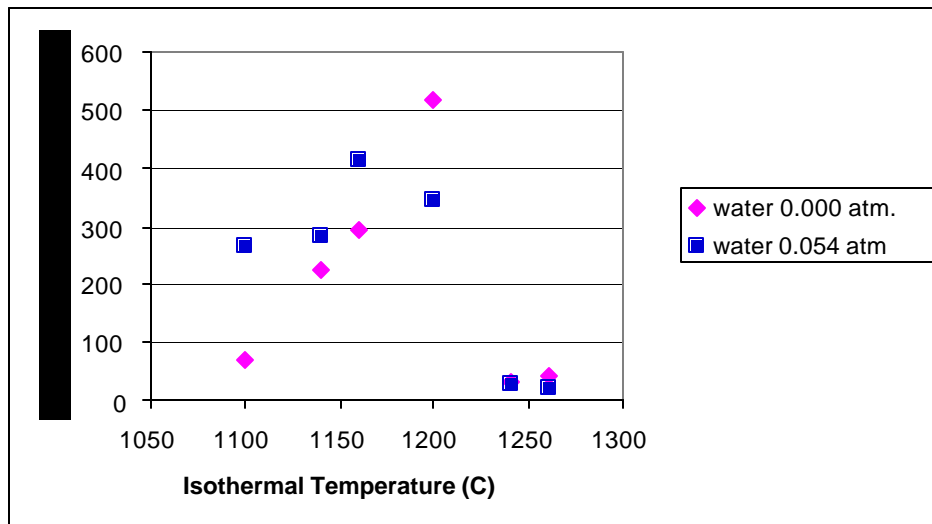


**Figure 26: The relationship between Growth Velocity and Isothermal Temperature of the Sample from Moisture and Moisture-free Conditions .**

Figure 26 shows the relationship between growth velocity and isothermal temperature of the sample from moisture and moisture-free conditions. Water enhances growth velocity only when isothermal temperature is lower than 1200°C (Figure 26).

The major finding of this study is the elimination of the effect of water vapor on solidification by the addition of MgO.

**Objective 5: Develop the ability to understand slag solidification under the conditions that occur in a continuous caster**

The CON1D model developed by Brian G. Thomas' group at the University of Illinois at Urbana-Campaign was used to predict the steel shell temperature and mold wall of hot face temperature for continuous casters. In Figure 27, the temperature profile for an industrial caster is shown. In this temperature profile, the temperature for the hot face drops to 1200°C in a few seconds, and then cools at a slower rate until the end of the mold. Figure 28 shows the temperature profile of the hot face together with TTT curve for the onset of crystallization for two different slags, experimental mold slag sample E3 and industrial mold slag sample STSP 816 (please note the change of appearance of the temperature profile due the change from linear to logarithmic scale of the x-axis).

The TTT curve predicts the onset of crystallization for the experimental mold slag E3 at 9s and 1155°C, while for sample STSP 816, no crystallization is expected. Slag samples of both slags were run through the calculated temperature profile for the hot face. For sample E3, crystals appeared in the sample at 9s, and at a distance of 0.2 mm from the thermocouple mimicking the hot face. The experimental image of the onset of crystallization is shown in Figure 29. Although, the TTT diagram in this case correctly predicted the time for the crystallization, the crystals should precipitate at the thermocouple and not 0.2 mm away. In Figure 30, the steel shell surface temperature is plotted with the CCT curve. In Figure 30, the cooling path of the steel shell does not intersect with the CCT curve and no crystallization is expected to occur at the thermocouple, which was observed. For sample STSP 816, no crystallization occurred as expected. The sample remains an undercooled liquid during the complete run. This is in good agreement with the result from the continuous cooling experiments with STSP 816. The results indicate that the TTT and CCT curves are powerful tools for comparing the crystallization behavior of different slags. However, it requires knowledge of the mold conditions and especially the temperature profile of the steel shell surface. Therefore, it cannot be concluded whether the TTT or the CCT curves give the most realistic picture of the crystallization behavior. It all depends on the specific thermal conditions the slag suffers in the caster.



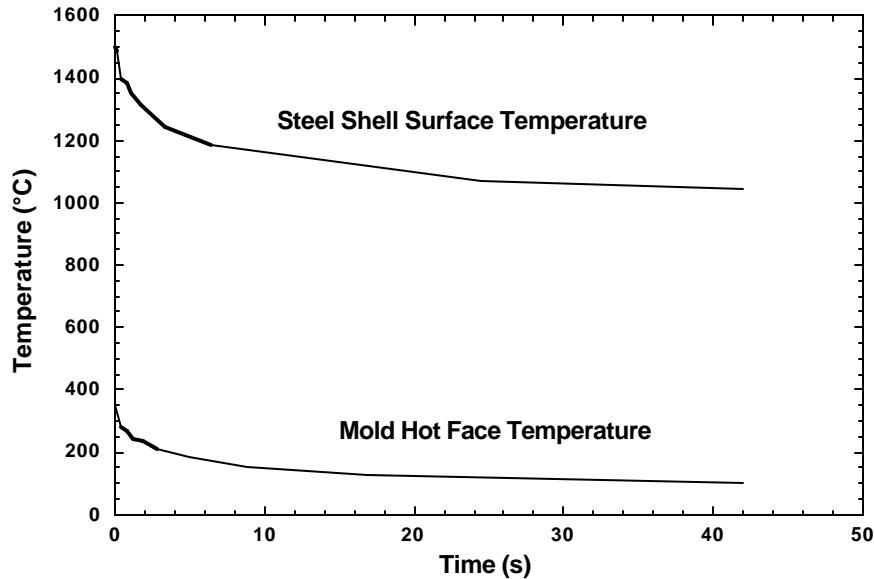


**Figure 27. Predicted Gap Temperatures for an Industrial Slab Caster.**

If sample E3 had been used during casting, one could suspect that the liquid slag film close to the strand would have crystallized at the bottom of the mold, especially since water vapor from the cooling spray can penetrate the gap between the mold wall and the strand at the bottom of the mold, increasing the extent of crystallization. The increased friction caused by a solid slag layer increases the wear on the mold shortening the life length of the mold, subsequently decreasing the productivity.

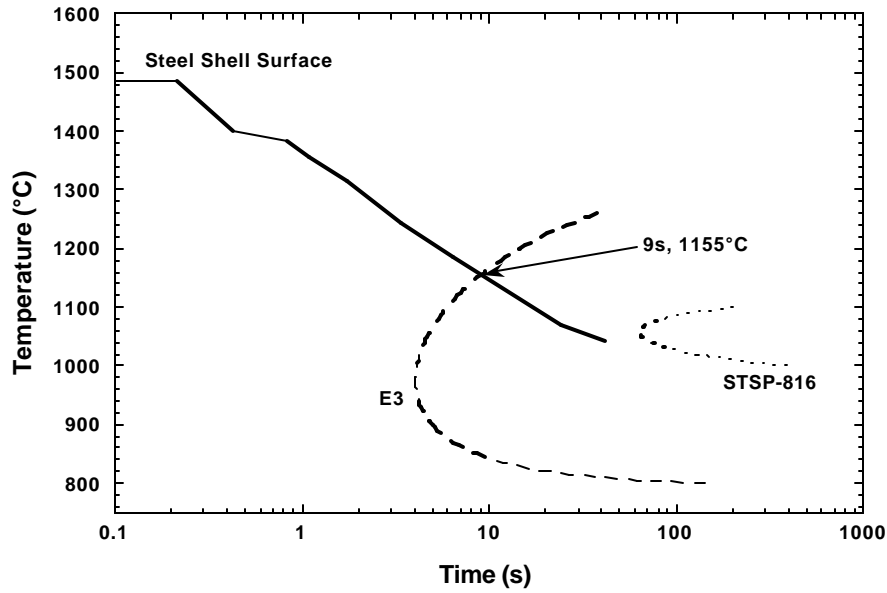


**Figure 28: Predicted Steel Shell Temperature together with TTT Curves for E3 and STSP 816.**

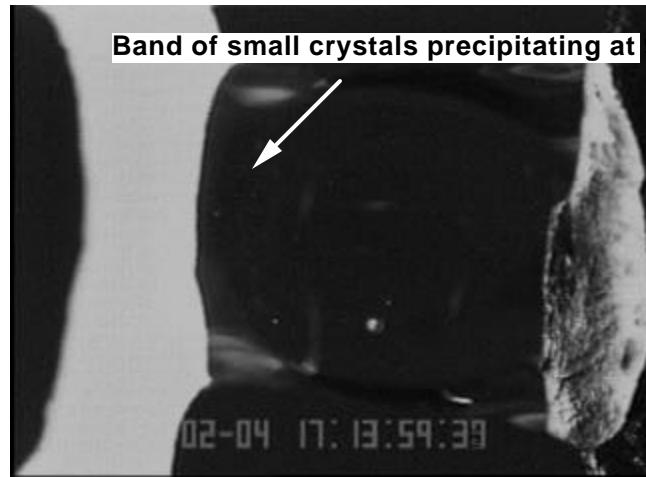


**Figure 29: The Onset of Crystallization for Sample E3 when Run Through the Temperature Time Profile of the Hot Face of the Columbus Stainless Caster.**

An intriguing part of designing a mold powder is to specify which crystalline phase(s) will precipitate. If only one crystalline phase can be allowed to precipitate, one can control the maximum fraction of crystalline fraction in the slag layer between the mold wall and the strand. Industrial samples of STSP-816 were collected from the mold during operation, and subsequently analyzed for composition and crystalline phases. The comparison of composition of STSP 816 before and after being used in casting operations is shown in table 3.

**Table 3: Composition of STSP 816 Before and After Use (wt%).**

Sample	CaO	SiO <sub>2</sub>	Al <sub>2</sub> O <sub>3</sub>	MgO	MnO	F	FeO	Na <sub>2</sub> O	Cr <sub>2</sub> O <sub>3</sub>	TiO <sub>2</sub>	K <sub>2</sub> O
Before	34.1	38.36	4.63	0.33		7.8	0.52	7.75			0.08
After	32.1	40.2	5.23	1.16	1.57	5.7	0.78	8.97	2.29	0.99	.110

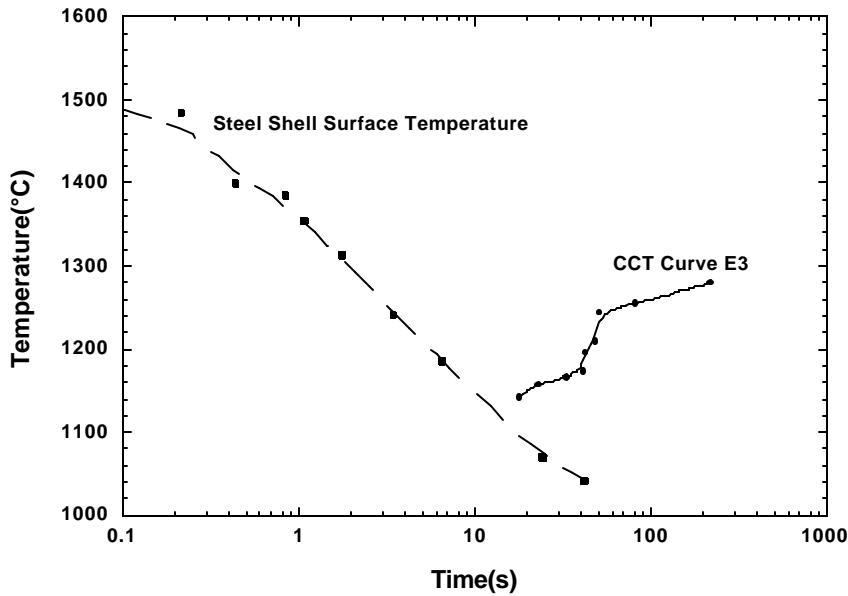


**Figure 30. Predicted Steel Shell Temperature together with CCT Curve for Sample E3.**

The compositional difference between before and after use is small. The slag has picked up Cr<sub>2</sub>O<sub>3</sub>, MnO, TiO<sub>2</sub>, and some Al<sub>2</sub>O<sub>3</sub> during use. To identify any crystalline phase, X-ray diffraction pattern of the used sample was obtained. The X-ray diffraction pattern of the used STSP-816 sample is shown in Figure 31.

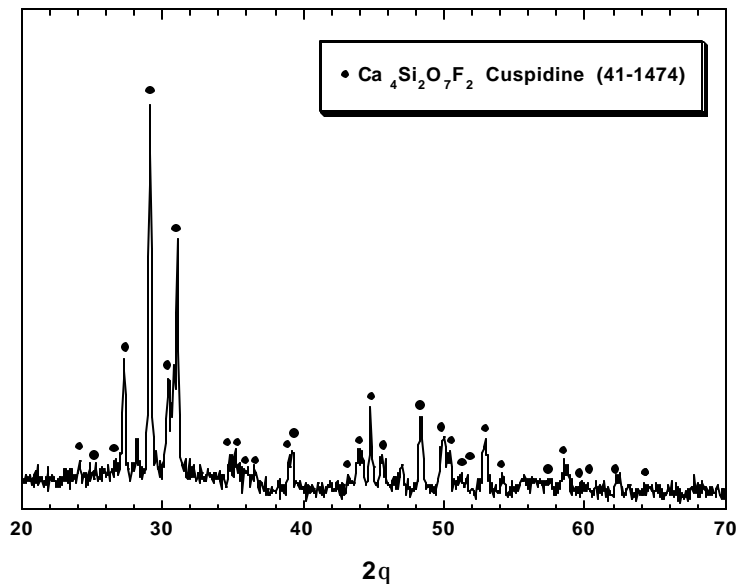


**Figure 31. X-ray Diffraction Pattern of STSP 816 Sample Collected from the Mold.**

It was determined that the precipitated crystalline phase was Cuspidine. Cuspidine has the following chemical formula  $\text{Ca}_2\text{Si}_2\text{O}_7\text{F}_2$ , and contains 45.9 wt% CaO, 32.8 wt%  $\text{SiO}_2$ , and 21.3 wt%  $\text{CaF}_2$  or 10.3 wt% F. By comparing the composition of Cuspidine with the composition of sample STSP 816 after use, it is obvious that the amount of Cuspidine is limited by the fluorine content. Simple mass balance reveals that the maximum achievable fraction of Cuspidine is 50.8 %. The  $\text{SiO}_2$  content of the remaining liquid at 50.8% crystalline fraction is increased to 48% resulting in a more viscous liquid. By increasing the fluorine content of the slag, the maximum crystalline fraction of Cuspidine can be increased. In most studies on collected samples of mold slag from the casters, Cuspidine has been the dominant crystalline phase. By adjusting the slag components that do not participate in the formation of Cuspidine, the formation of a secondary crystalline phase ( $\text{NaAlSiO}_4$ ,  $\text{Na}_2\text{Ca}_3\text{Si}_2\text{O}_8$  and  $\text{Ca}_2\text{Al}_2\text{SiO}_7$ ) can be enhanced or suppressed.

An industrial participant in this project used a CLU vessel, which utilized steam for the decarburization process. During a time of steam leaks due to a faulty valve, there were several consecutive breakouts. It was found that the hydrogen levels of the steel increased in the melt during this period with steam leaks to the melt. The heat flux was monitored for the period of steam leaks, and compared to normal operations. The comparison in heat flux can be seen in Figure 32. Figure 32 shows clearly that the heat flux decreased during the period when the steam leaks occurred.

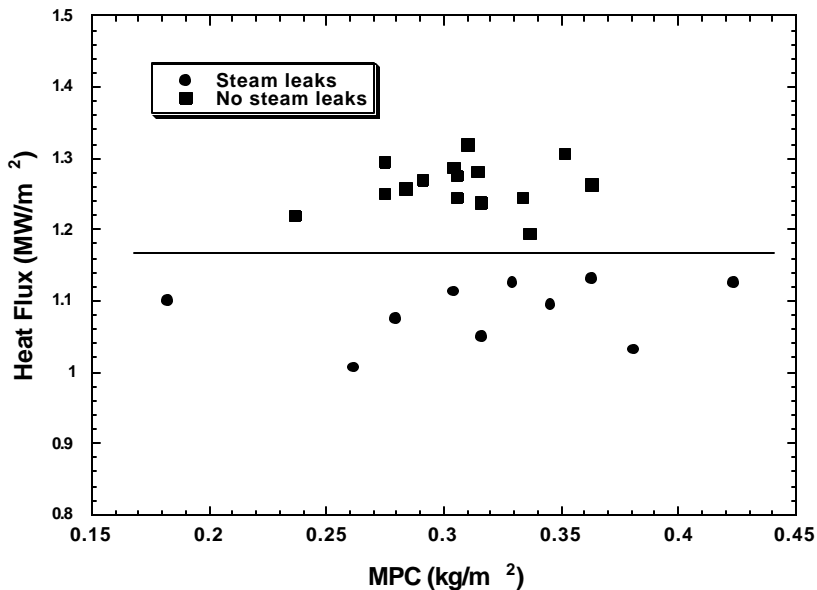


**Figure 32: Comparison of Measured Heat Flux of the Wideface of the Caster between Period of Steam Leaks and No Steam Leaks.**

Hydrogen has low solubility in solid steel compared to liquid steel; so upon solidification, hydrogen will precipitate at the solidification front. As the shell forms in continuous casting, the hydrogen gas can either dissolve back into the remaining liquid in the core of the strand, or be pushed out in the mold slag layer adjacent to the strand surface. The presence of gas in the slag layer will cause a reduction of the heat transfer. Another reason for reduced heat flux is increased crystallization of the used mold slag. The presence of hydrogen was found to not increase the extent of crystallization and can probably not account for any increased crystallization of the slag layer. Reducible oxides such as FeO and MnO are readily available on the strand surface, but also in the mold slag in less quantity. The reduction reaction of these oxides with hydrogen will form H<sub>2</sub>O(g) as a product. Water vapor, even in small quantities, causes a dramatic increase in the crystallization of mold slags. Increased crystallization of the liquid mold slag layer will cause the heat flux to decrease, and the friction between mold wall and strand to increase, which is a sure recipe for a break out to occur.

Another industrial participant, when casting of round billets, found drag marks, caused by increased friction, on the surface of billets when using mold powder that has been exposed to the ambient atmosphere for a longer time. Mold powders contain components (CaO, Na<sub>2</sub>O) that easily pick up significant amounts of moisture from the atmosphere. Water can be present in mold powders, as free moisture or as crystalline water. When measuring water content of mold powders it is assumed that water detected above 900°C is in the form of crystalline water. The temperature gradient in the liquid slag pool on top of the liquid steel ranges approximately from 1150°C (melting point of the mold slag) at the bottom of the sintered layer to 1550°C at the steel surface. This temperature gradient will cause strong convection to occur in the molten slag pool. During melting experiments with slags in this study, bubble formation was observed, and the retention

time of bubbles could last up to a minute even for low viscous slags. With excess water content of the mold powder, the bubble formation during the melting will most likely increase, and with the convection present in the molten slag pool, bubbles of moisture are withdrawn into the gap between strand and mold wall. The presence of moisture increases the crystallization rate of the lubricating slag layer resulting in higher friction forces on the surface of the cast product.

One of the functions of the mold slag is to dissolve/absorb solid/liquid inclusions that are separated out from the steel in the mold. Mold slags are generally very effective in dissolving solid oxide inclusions due to the high content of fluorides and  $\text{Na}_2\text{O}$ . However, large inclusions may not completely dissolve and can end up in the liquid slag layer. Solid oxide particles in liquid slags are potent sites for heterogeneous nucleation and can decrease the incubation time for the onset of crystallization. A 0.1 mm layer of liquid slag could, therefore, crystallize in less than 10 seconds. The reduction of incubation time for the onset of crystallization caused by the presence of solid oxides could very well affect the casting operation.

Thus this work, as well as giving the ability to measure slag solidification, also allows the solidification behavior of casters to be predicted. It is interesting to note that changing the atmospheres had a more dramatic change to the crystallization behavior than changes in the composition for the slag system studied in this project. The atmospheric conditions around the mold slag in this study are not normally found in casting operations. However, the results still clearly point out that the surroundings of the mold slag strongly affect the crystallization temperature and crystal growth rate, and subsequently, its function as lubricant and medium for heat transfer.

#### Objective 6: Develop an ability to predict the solidification behavior of slags

From the isothermal experiments with the DHTT, the growth rate and the crystallization time for different crystallization temperatures were directly measured as shown in Figure 33.

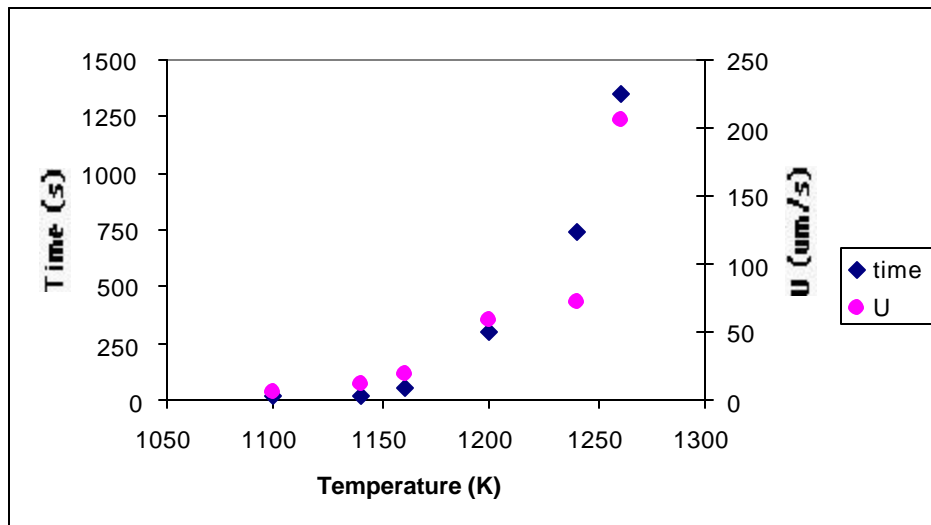


**Figure 33: The Relationship between the Growth Rate (U) and the Crystallization Time of a Eutectic  $\text{CaO-Al}_2\text{O}_3$  Slag at Different Temperatures.**

Uhlmann predicted crystallization time by calculating the nucleation and growth rate and substituting for volume fraction in Johnson-Mehl-Avrami equation. In this work, nucleation rate was calculated by substitution of the growth rates and crystallization time into Johnson-Mehl-Avrami equation. In addition, the solid-liquid interfacial energy was calculated from nucleation rate.

The Johnson-Mehl-Avrami equation can be written as follows:

$$X = \frac{p}{3} IU^3 t^4 \quad (1)$$

Where

X is just detected crystalline phase.

I is nucleation rate ( $\#/m^3 \cdot s$ ).

G is growth rate (m/s)

t is time when crystallization start or crystallization time (s).

When  $X=10^{-6}$ , the nucleation rate (I) can be calculated from:

$$I = \frac{3 \cdot X}{p \cdot U^3 \cdot t^4} \quad (2)$$

The calculated values of nucleation rate at different temperatures are shown in Figure 34.

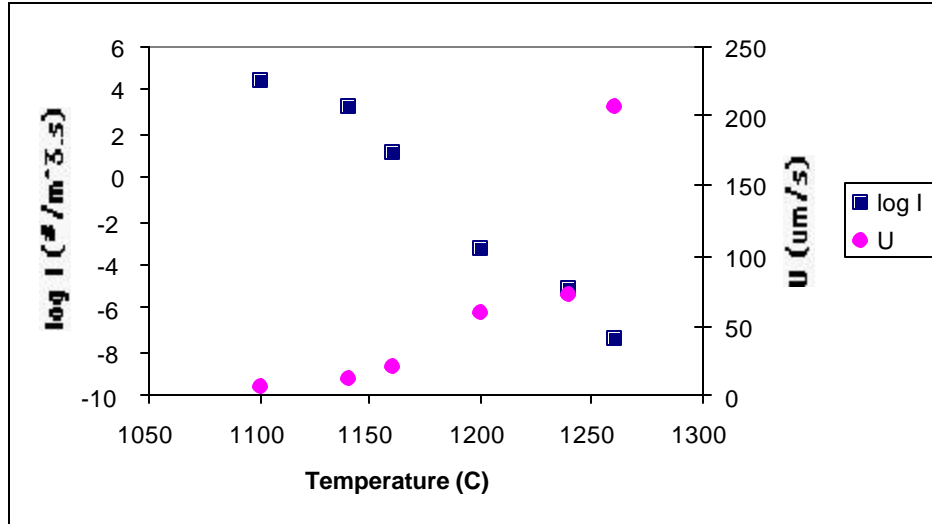


**Figure 34: The Relationship between the Measured Growth Rate and the Calculated Nucleation Rate of a Eutectic CaO-Al<sub>2</sub>O<sub>3</sub> Slag at Different Temperatures.**

If homogeneous nucleation is assumed, the nucleation equation is:

$$I = \frac{N_v \cdot k \cdot T}{3 \cdot p \cdot a^3 \cdot h} \exp\left(-\frac{\Delta G^*}{kT}\right) \quad (3)$$

Where

$N_v$  is number of molecule per unit volume ( $\#/m^3$ ).

k is Boltzmann constant (J/K)= $1.38 \times 10^{-23}$  (J/K).

a is molecular diameter (m).

$\eta$  is viscosity (Pa.s).

$\Delta G^*$  is kinetic barrier of nucleation (J) and can be written as follows:

$$\Delta G^* = \frac{16p}{3} \cdot \frac{(g_{sl})^3}{(\Delta G_v)^2} \quad (4)$$

Where

$\gamma_{sl}$  is the surface energy between solid and liquid (J/m<sup>2</sup>).

$\Delta G_V$  is the volume free energy difference between solid and liquid (J/m<sup>3</sup>).

And

$$\Delta G_V = \frac{\Delta G}{V} \quad (5)$$

Where

$\Delta G$  is free energy difference between solid and liquid (J/mol).

$V$  is molar volume (m<sup>3</sup>/mol).

From equation 3 and 4, solid-liquid interfacial energy can be calculated as:

$$g_{sl} = \sqrt[3]{\frac{-3kT}{16p} \cdot (\Delta G_V)^2 \cdot \ln\left(I \cdot \frac{3p \cdot a^3 \cdot h}{N_v \cdot kT}\right)} \quad (6)$$

For a eutectic CaO-Al<sub>2</sub>O<sub>3</sub> slag.

$V = 28 \times 10^{-6}$  (m<sup>3</sup>/mol)

$N_v = 1.67 \times 10^{29}$  (#/m<sup>3</sup>)

$a = 2.5 \times 10^{-10}$  (m)

The viscosity of the eutectic CaO-Al<sub>2</sub>O<sub>3</sub> slag can be express as  $\eta = 10^{\frac{3.56 \cdot 10^4}{T} - 16.47}$  (Pa.s) for temperatures between 1527°-1777°C. To determine the viscosity between 1100°-1300°C, an extrapolation of this equation was used. This extrapolation seems reasonable because the extrapolated viscosity approaches 10<sup>12</sup> Pa.s (viscosity of glass) at 970°C, which is closed to glass transition temperature of CaO-Al<sub>2</sub>O<sub>3</sub> slag (Figure 35).

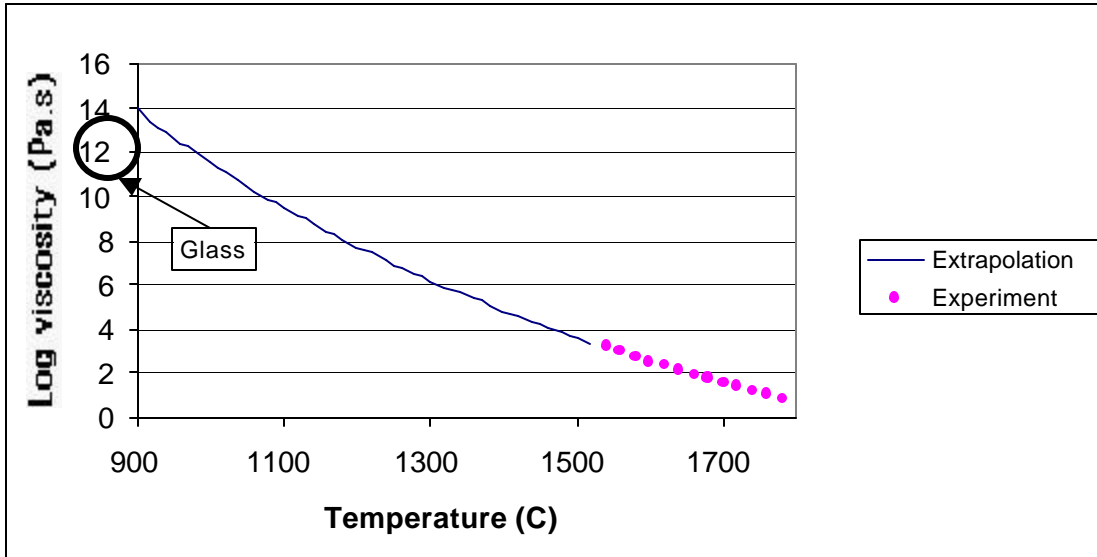


**Figure 35: The Viscosity of CaO-Al<sub>2</sub>O<sub>3</sub> Slag**

For small undercoolings, the free energy difference between solid and liquid ( $\Delta G$ ) is usually approximated by the expression  $\Delta G \approx \Delta H_f \frac{(T_L - T)}{T_L} \approx \Delta S_f (T_L - T)$ . For high

undercooling, this relationship between  $\Delta G$  and  $\Delta T$  must be corrected. In this work,  $\Delta G \approx T \cdot \Delta S_f \frac{(T_L - T)}{T_L}$  (J/mol.) was used. The entropy of formation solid ( $\Delta S_f$ ) was



calculated with FACT thermochemistry software and was  $\Delta S_f = 32 \text{ J/mol.K}$  (as shown in Figure 36).

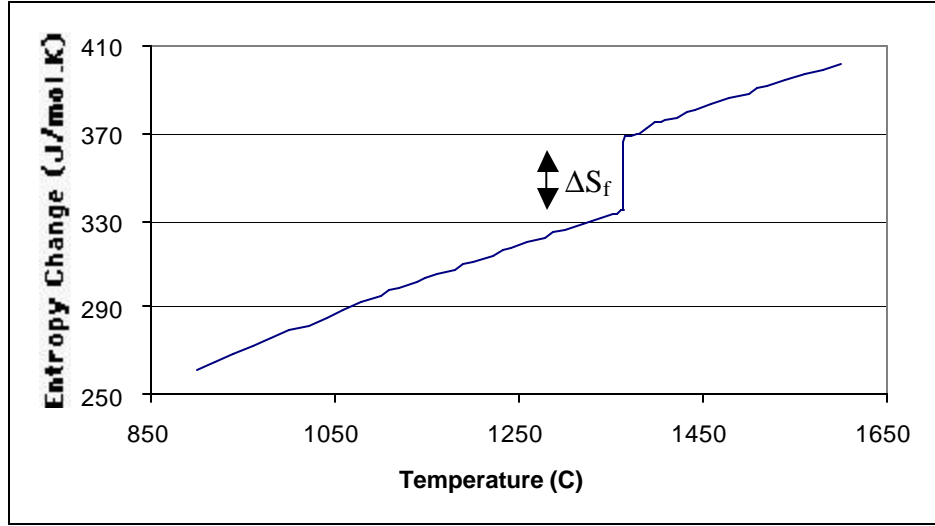


**Figure 36: The Relationship between Entropy Change and Temperature of Eutectic CaO-Al<sub>2</sub>O<sub>3</sub> Slag.**

The solid-liquid interfacial energy of eutectic CaO-Al<sub>2</sub>O<sub>3</sub> slag was calculated with the Equation 6 as shown in Figure 37. From Figure 37, the solid-liquid interfacial energy depends on the temperature as per the following expression:

$$g_{sl}(\text{J} / \text{m}^2) = 0.3998 - 0.002 \bullet T(\text{C}) \quad (7)$$

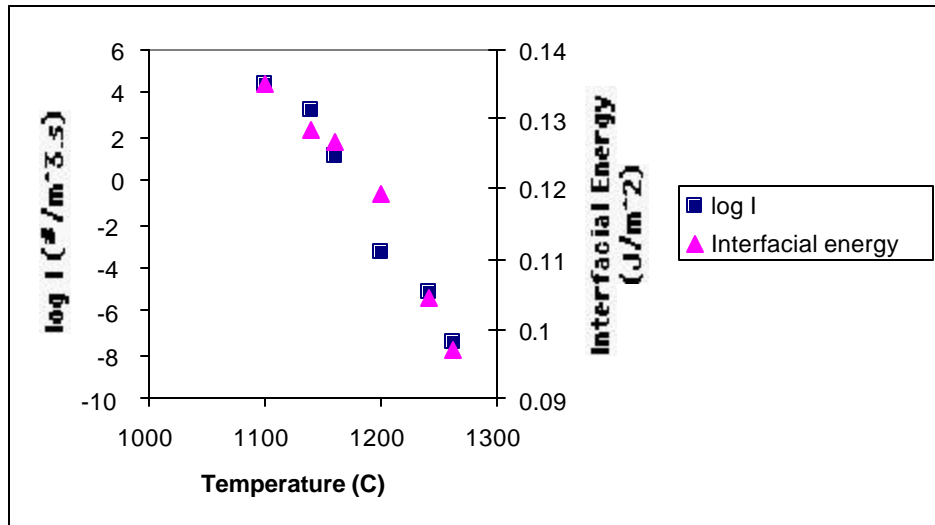


**Figure 37: The Relationship between Nucleation Rate and Solid-Liquid Interfacial Energy of Eutectic CaO-Al<sub>2</sub>O<sub>3</sub> Slag for Different Temperature.**

In this work, the effect of heterogeneous nucleation on solid-liquid interfacial value can be investigated if the contact angle between a CaO-Al<sub>2</sub>O<sub>3</sub> slag and a platinum substrate is known.

For Homogeneous Nucleation

$$I^{HO} = \frac{N_v \cdot k \cdot T}{3 \cdot p \cdot a^3 \cdot h} \exp\left(-\frac{\Delta G^*}{kT}\right) \quad (8)$$

For Heterogeneous Nucleation

$$I^{HE} = \frac{N_s \cdot A_v \cdot k \cdot T}{3 \cdot p \cdot a^3 \cdot h} \exp\left(-\frac{\Delta G^*}{kT}\right) \cdot f(q) \quad (9)$$

Where

$N_s$  is the number of molecules per unit area of substrate (#/m<sup>2</sup>).

$A_v$  is the area of nucleating substrate per unit volume of the melt (1/m).

$$I_{Total} = I^{HO} + I^{HE} \quad (10)$$

Assume

$$N_v = N_s \cdot A_v$$

$I^{HE} \gg I^{HO}$  because at temperature above the nose of TTT curve, the crystallization always occur on the surface of thermocouple.

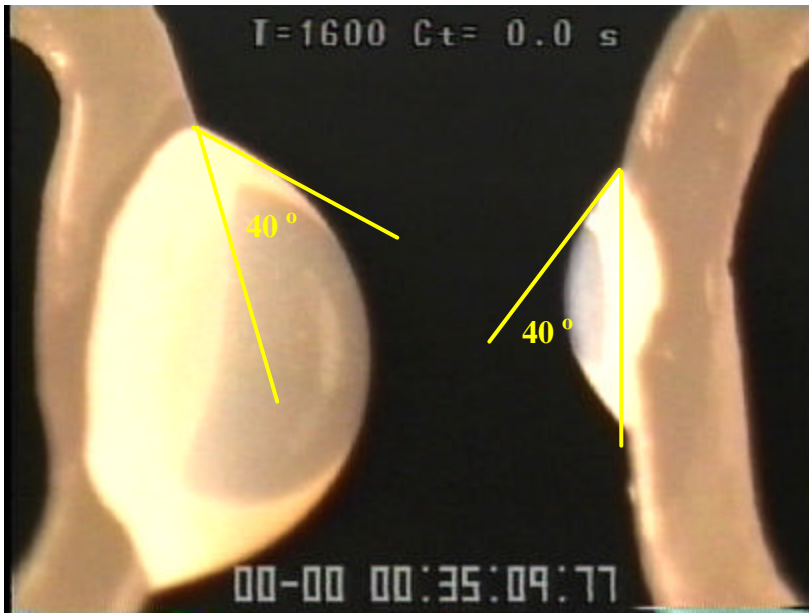
Then

$$I_{Total} = I^{HE} = I$$

Therefore

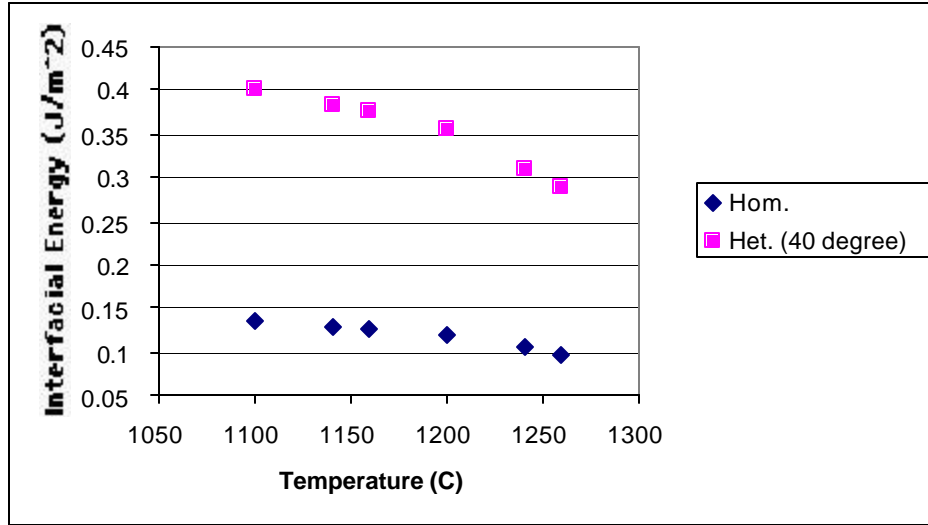
$$g_{sl} = \sqrt[3]{\frac{-3kT}{16p} \cdot \frac{(\Delta G_v)^2}{f(q)} \cdot \ln\left(I \cdot \frac{3p \cdot a^3 \cdot h}{N_v \cdot kT}\right)} \quad (11)$$

Figure 38 shows the shape of liquid CaO-Al<sub>2</sub>O<sub>3</sub> slag on the surface of B-type thermocouples. From Figure 38, contact angle is approximately 40°.



**Figure 38: The Droplets of Liquid CaO-Al<sub>2</sub>O<sub>3</sub> Slag on the Surface of B-type Thermocouples at 1600°C**

The effect of heterogeneous nucleation on the value of solid-liquid interfacial energy is shown in Figure 39. From Figure 39, the value of solid-liquid interfacial energy from heterogeneous nucleation is almost triple of the value from homogeneous nucleation.



**Figure 39: The Effect of Heterogeneous Nucleation on the Value of Solid-Liquid Interfacial Energy.**

From Figure 39, the solid-liquid interfacial energy under heterogeneous nucleation depends on the temperature by:

$$g_{sl}(J/m^2) = 1.1893 - 0.0007 \cdot T(C) \quad (12)$$

The solid-liquid interfacial energy from heterogeneous nucleation was used in Uhlmann's method to estimate TTT curve for different contact angles. The result is shown in Figure 40. This shows that changing the contact angle by only  $10^\circ$  affects the position and shape of the TTT curve. Thus the solidification behavior of  $\text{CaO-Al}_2\text{O}_3$  will be very sensitive to the presence of nucleating agents.

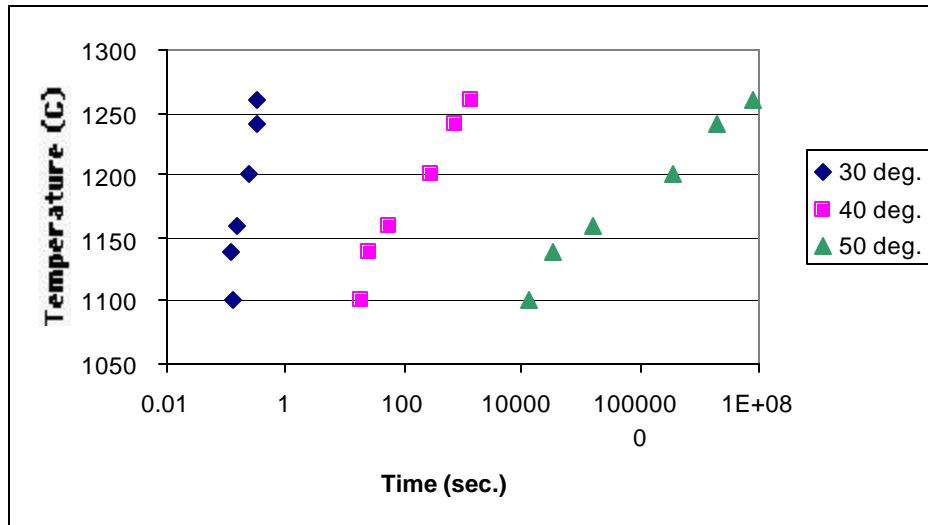


**Figure 40: The Effect of Heterogeneous Nucleation on TTT Curve.**

The same calculation method and parameters were used for the eutectic  $\text{CaO-Al}_2\text{O}_3$  slag with 0.042% water. Dissolved water causes a decrease in the viscosity. Since there is no data for the viscosity of the eutectic  $\text{CaO-Al}_2\text{O}_3$  slag with 0.042% water, then the degree of decrease in viscosity of  $\text{LiO} \cdot 2\text{SiO}_2$  was used in the eutectic  $\text{CaO-Al}_2\text{O}_3$ -0.042% water slag as shown in Figure 41.

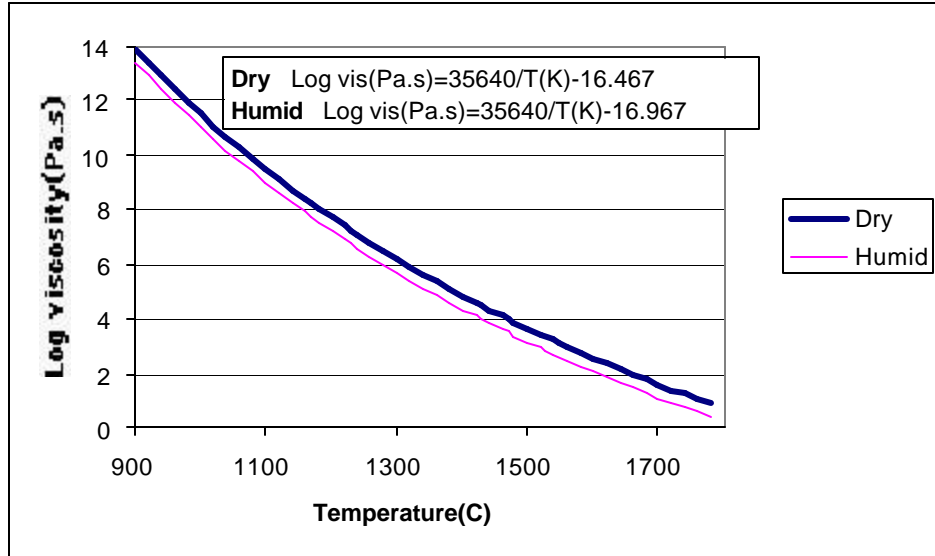


**Figure 41: The Viscosity of  $\text{CaO-Al}_2\text{O}_3$  Slag under Dry and Humid Atmosphere.**

From the growth rate and crystallization time for different temperature in Figure 42, nucleation rate of  $\text{CaO-Al}_2\text{O}_3$ -0.042% water slag were calculated and shown in Figure 43.

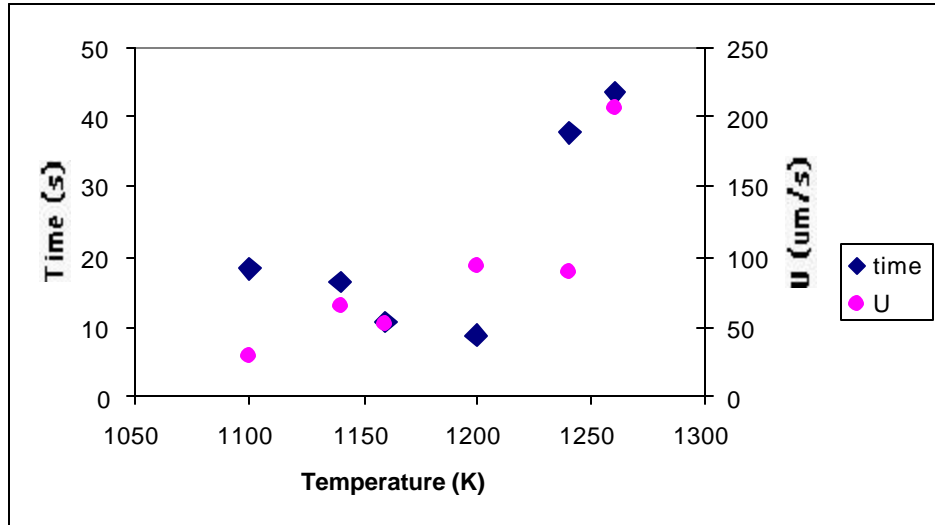


**Figure 42: The Relationship between Growth Rate and Nucleation Time of Eutectic  $\text{CaO-Al}_2\text{O}_3$ -0.042% Water Slag for Different Temperatures**

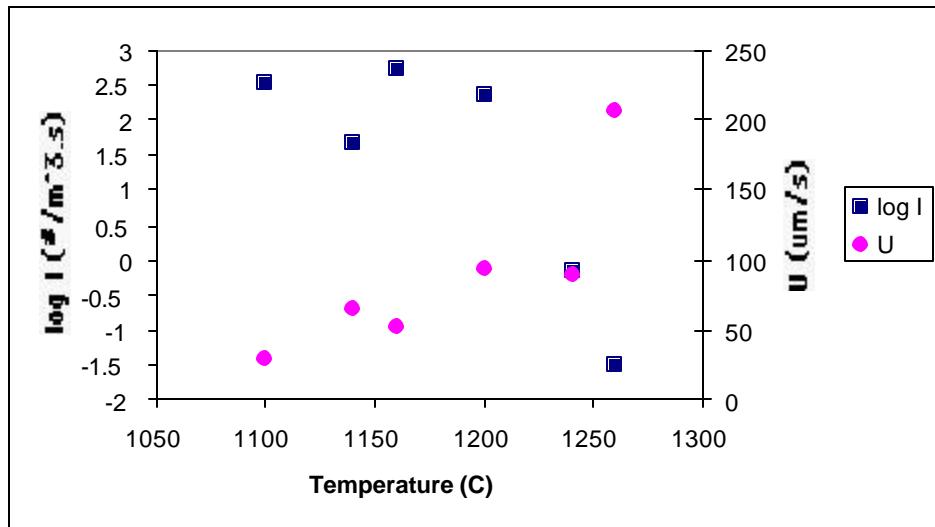


**Figure 43: The Relationship between Measured Growth Rate and Calculated Nucleation Rate of Eutectic  $\text{CaO-Al}_2\text{O}_3$ -0.042% Water Slag for Different Temperatures**

In this calculation, the heterogeneous nucleation was applied. Figure 44 shows that the contact angle changed from  $40^\circ$  under dry conditions to  $33^\circ$  under humid conditions. The solid-liquid interfacial energy was calculated and shown in Figure 45.

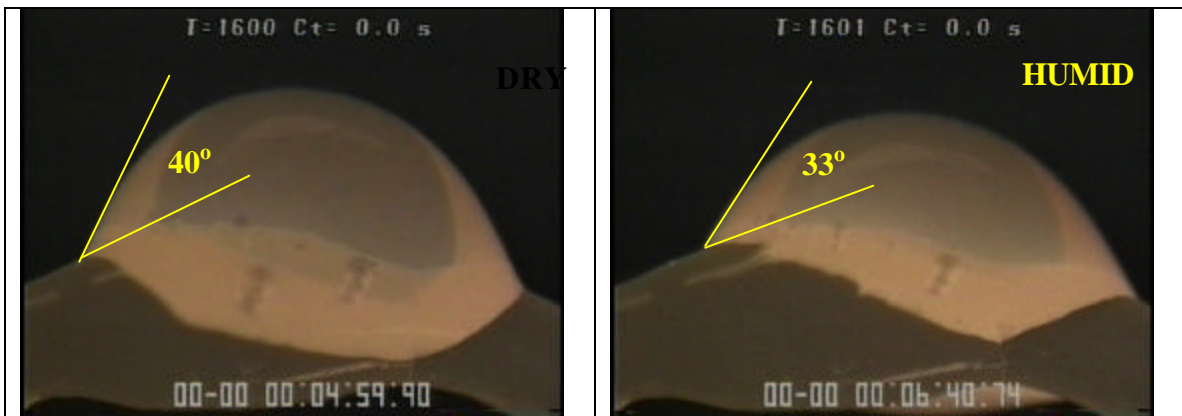


**Figure 44: The Effect of Humid Atmosphere on the Wettability of  $\text{CaO-Al}_2\text{O}_3$  Slag on the Surface of B-type Thermocouple.**

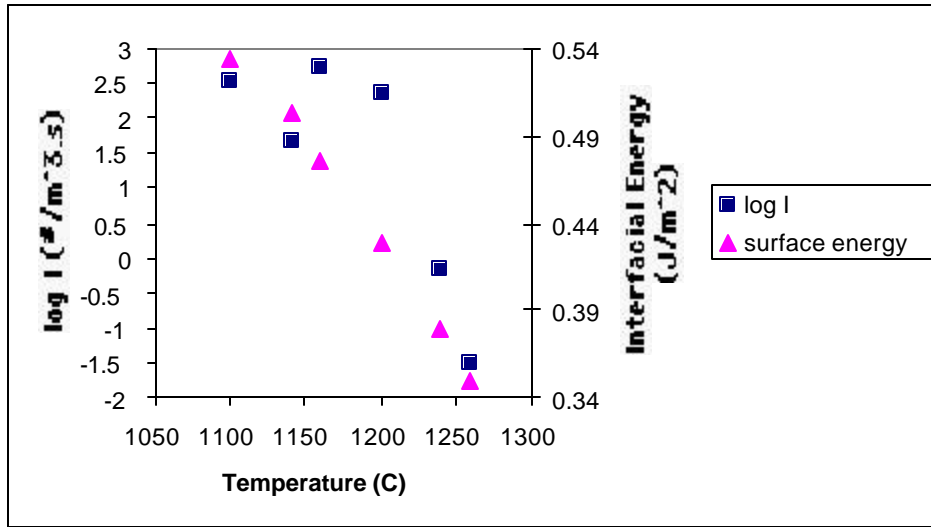


**Figure 45: The Relationship between Nucleation Rate and Solid-Liquid Interfacial Energy of Eutectic CaO-Al<sub>2</sub>O<sub>3</sub>-0.042%Water Slag for Different Temperature .**

From Figure 45, the solid-liquid interfacial energy depends on the temperature by:

$$g_{sl}(J/m^2) = 2.1473 - 0.0012 \cdot T(C)$$

From this mathematical analysis, it can be concluded that:

- The Uhlmann's method can be used for estimation of the nucleation rate of CaO-Al<sub>2</sub>O<sub>3</sub> slag and results in the reasonable values for solid-liquid interfacial energy of CaO-Al<sub>2</sub>O<sub>3</sub>.
- The value of the free energy of formation of CaO-Al<sub>2</sub>O<sub>3</sub> and the presence of heterogeneous nucleation agents can affect the calculated value of solid-liquid interfacial energy CaO-Al<sub>2</sub>O<sub>3</sub> slag. In this study, platinum as a nucleating agent, the solid-liquid interfacial energy appears to be:

$$g_{sl}(J/m^2) = 1.1893 - 0.0007 \cdot T(C)$$

- Water enhances crystallization of CaO-Al<sub>2</sub>O<sub>3</sub> slag by increasing the nucleation rate at a high temperature and increasing the growth rate at low temperature.
- Water also appears to increase the solid-liquid interfacial energy of CaO-Al<sub>2</sub>O<sub>3</sub> slag. The solid-liquid interfacial energy, in presence of water, can be represented as follows:

$$g_{sl}(J/m^2) = 2.1473 - 0.0012 \cdot T(C)$$

- It appears that water vapor affects solidification behavior in two ways: (1) It increases diffusion rate in the liquid ahead of growing interface due to segregation, and (2) It changes the solid-liquid interfacial energy of the

precipitating solid. Both of these affect results in a significant change to the TTT curve.

**Objective 7: Develop the criteria for optimization of slags in steelmaking environments where they are under thermal gradients**

This work has shown that we can measure the effect of slag chemistry and thermal gradients on the solidification behavior of slags. We can also determine the effect of atmospheric water vapor. Thus, this technique can be used to develop the criteria for optimization of slags in steelmaking environments where they are under thermal gradients.

An example of the manner in which this technique can be used can be seen when three experimental mold slags (table 4) were measured.

**Table 4: Composition of Experimental Mold Slags and Type of Experiment Performed.**

<b>Sample</b>	<b>%CaO</b>	<b>%SiO<sub>2</sub></b>	<b>%Al<sub>2</sub>O<sub>3</sub></b>	<b>%Na<sub>2</sub>O</b>	<b>%CaF<sub>2</sub></b>	<b>C/S</b>	<b>Experiment</b>
E1	45	41	7	7	0	1.1	Isothermal
E2	44.5	44.5	4	7	0	1.0	Isothermal
E3	39.58	40.94	6.94	9.57	1.00	0.97	Iso.,CC,DCT

The basicity ( $C/S = CaO/SiO_2$ ) in this study is defined as the lime silica ratio.

Figures 46, 47, and 48 show the TTT diagrams for Samples E1, E2 and E3, respectively. The time for the beginning of crystallization ( $t_{0.005}$ ) was defined as 0.5% crystalline fraction, considering the resolution of the observation system. The time for the end of crystallization ( $t_{0.95}$ ) was defined as 95% crystalline fraction.

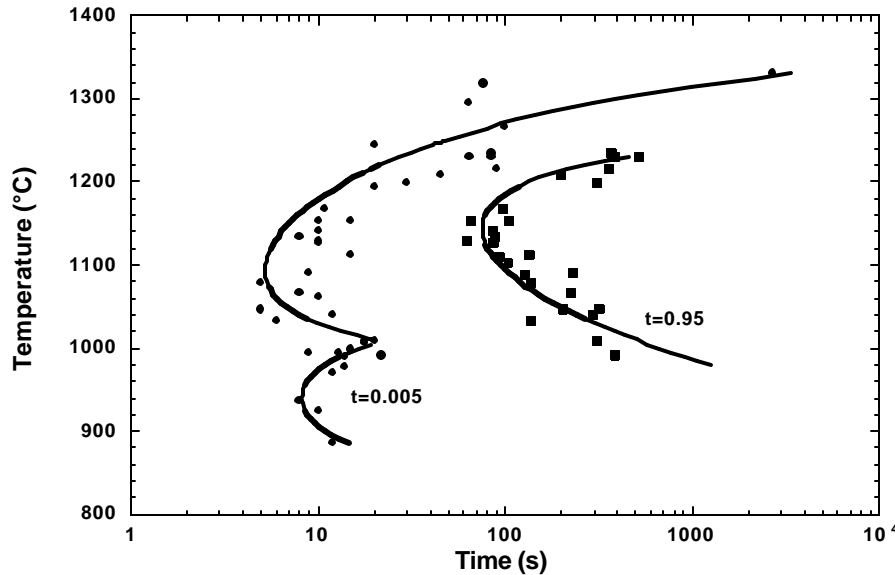


**Figure 46: TTT Diagram for Crystallization of Experimental Mold Slag Sample E1.**

During the melting experiments, it was found that Sample E1 became completely transparent at around 1330°C. Isothermal experiments near 1330°C showed that the beginning of crystallization took place after a relatively long time (~45 min.), and was never completed through the whole sample. The crystalline fraction remained in equilibrium with the liquid phase, crystals formed and dissolved simultaneously. 100% crystalline fraction could be observed at around 1240°C. This observation suggests that a two-phase region exists between approximately 1330°-1240°C. This TTT curve has an upper (1330°-1010°C) and lower nose (1010°-885°C). The nose positions occur at 1100°C and 930°C, respectively. The presence of this double nose was first questioned, as there is no change in the crystal phase along this curve. However, there is a change in crystal morphology at 1000°C that would explain the double nose due to a new nucleation mechanism.

For Sample E2, only one nose was observed at 1020°C and 15s. A two-phase region appeared between 1320°C and 1280°C. 100% crystalline phase was observed at lower temperatures.



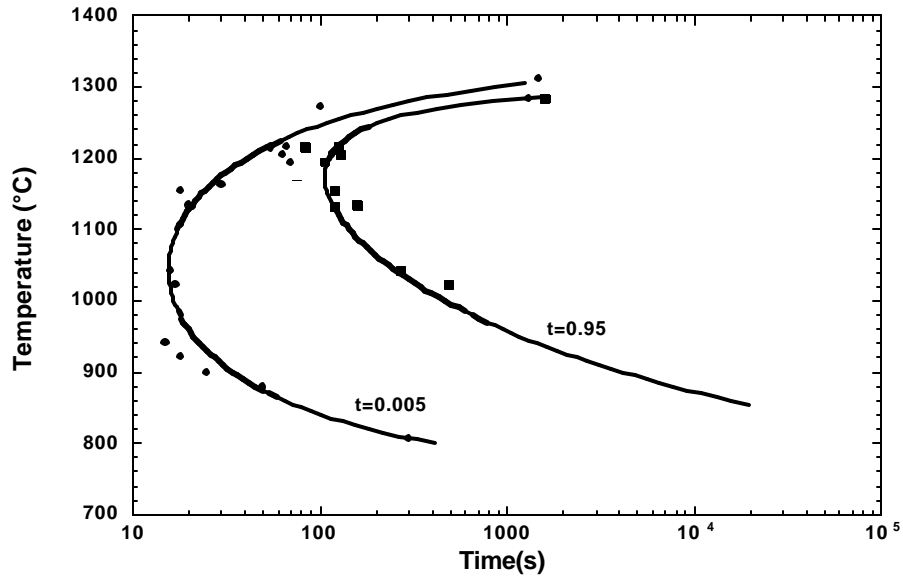


**Figure 47: TTT Diagram for Crystallization of Experimental Mold Slag Sample E2.**

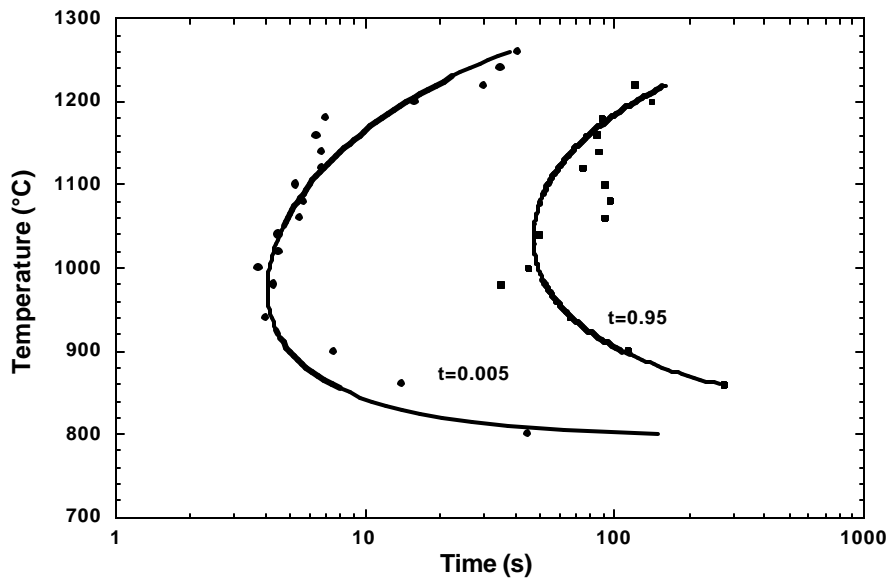


**Figure 48: TTT Diagram for Crystallization of Experimental Mold Slag Sample E3.**

For Sample E3, melting experiments were performed with a low heating rate to determine the solidus and liquidus temperatures. It was found that the sample started to melt at

1160°C, and became completely liquid at 1260°C. No crystallization was observed above 1260°C. From this result, it was concluded that a two-phase region exists between 1260°C and 1160°C. For Sample E3, the time for the beginning of crystallization is generally short (4-7s) between 1180°-940°C. The nose position is at 1000°C and 4s.

The beginning and end of crystallization at different temperatures forms a C-shaped curve for all Samples, as predicted by the classical nucleation theory. The obtained TTT diagrams for the onset of crystallization were compared with the TTT diagram obtained by Kashiwaya et al for the Sample with 7% Na<sub>2</sub>O in Figures 49-51.

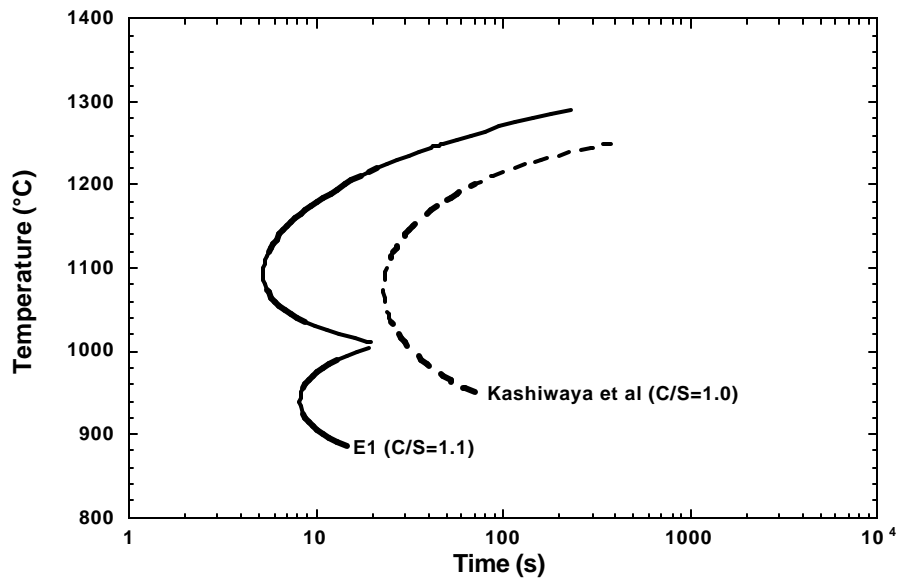


**Figure 49: Comparison of the Beginning of Crystallization for Mold Slags with Different Ratios of CaO and SiO<sub>2</sub>.**

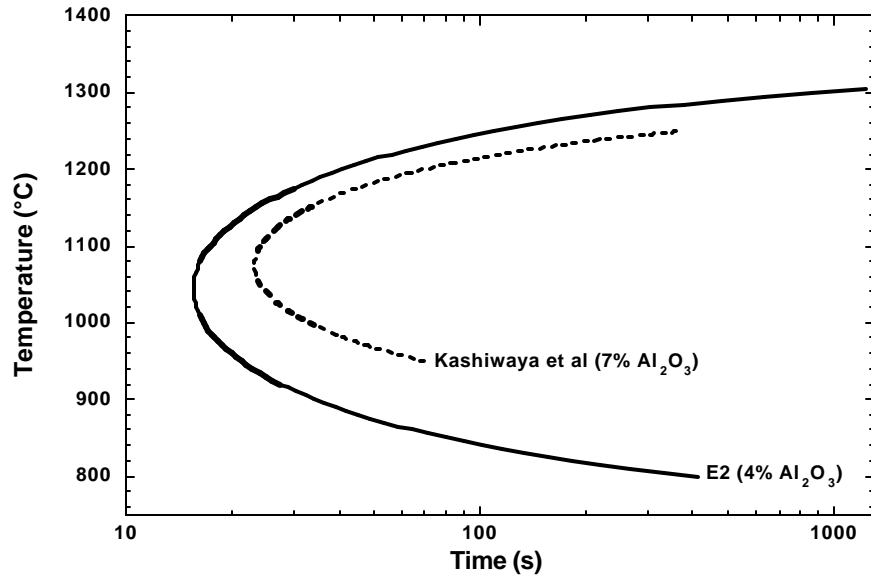


**Figure 50. Comparison of the Beginning of Crystallization for Mold Slags with Different Contents of  $\text{Al}_2\text{O}_3$ .**

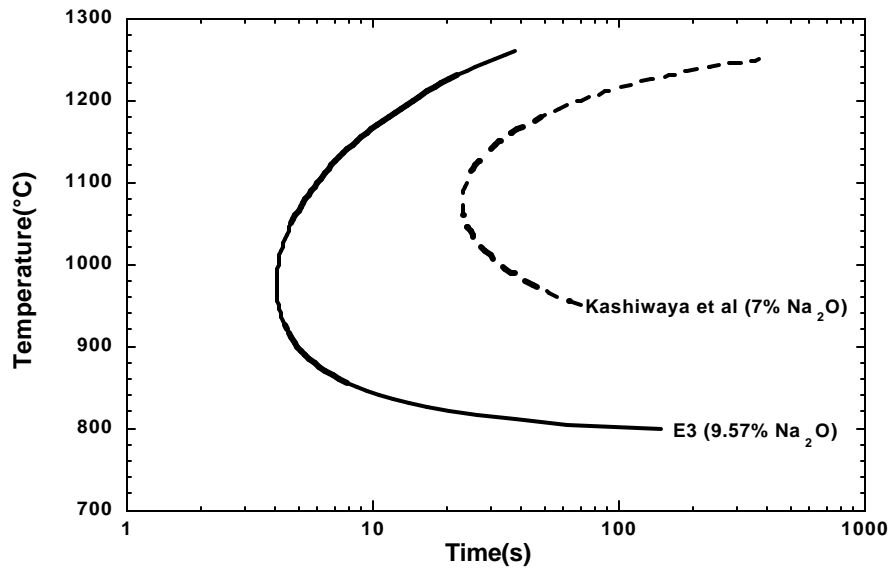


**Figure 51: Comparison of the Beginning of Crystallization for Mold Slags with Different Contents of  $\text{Na}_2\text{O}$ .**

The Sample in the Kashiwaya et al study was examined in a smaller temperature range than for the current study. The effect of increasing the basicity (Sample E1), i.e. the content of  $\text{CaO}$  is shown in Figure 49. Increasing the basicity reduces the time for the beginning of crystallization. The result that increasing the basicity fits well with the

theory that lime promotes crystallization by increasing the liquidus temperature and decreasing viscosity. The free amount of oxygen anions is favored by higher basicity. Due to the higher liquidus temperature, the undercooling increases for the same temperature, resulting in a higher nose position of the curve for Sample E3.

The lower content of alumina also decreases the time for the onset of crystallization, especially below 1100°C as shown in Figure 50. Alumina is an amphoteric oxide and has been reported at low concentrations to promote a glassy network upon cooling. Reductions of alumina would therefore decrease the viscosity, making mass diffusion faster. This would also increase crystallization as mass diffusion can be assumed to be the rate-controlling step for crystallization.

Comparing Sample E3 with the Sample from Kashiwaya et al. in Figure 51, it is found that increasing the content of  $\text{Na}_2\text{O}$ , and adding a small amount  $\text{CaF}_2$  increases the crystallization quite significantly. This is in good agreement with the conclusions of Kashiwaya on the effect of  $\text{Na}_2\text{O}$  on crystallization behavior. The effect of  $\text{Na}_2\text{O}$  is clarified in Figure 52. The increased crystallization rate with increasing  $\text{Na}_2\text{O}$  content is in good agreement with previous studies. A comparison of the samples in the current study is shown in Figures 52. The incubation time for the onset of crystallization was shorter for both Samples E1 and E2 compared to the samples studied by Kashiwaya.

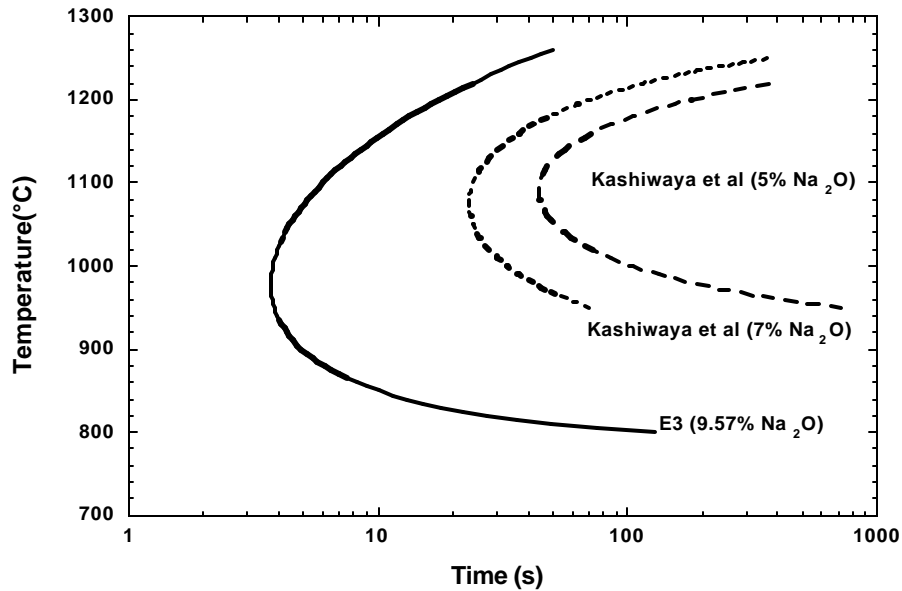


**Figure 52: TTT Curves showing the Effect of  $\text{Na}_2\text{O}$  on the Incubation Time for the Onset of Crystallization.**

The effect of cooling rate on the crystallization of a slag during continuous cooling with a thermal gradient was studied for Sample E3. The time for the beginning of the crystallization was almost the same for all experiments, ~10s. The first crystals to precipitate were very small (cloud), and as the cooling continued, faceted columnar and equiaxed crystals appeared in the Sample. A schematic representation of the positions of different crystal morphologies within the Sample can be seen in Figure 53.

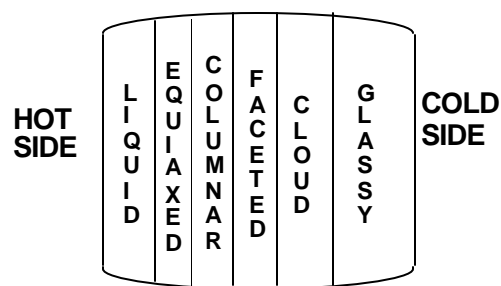


**Figure 53. Schematic Representation of Morphological Layers in the Sample.**

The morphology of the crystals makes it possible to estimate the degree of undercooling for different regions in the Sample. The amount and appearance of the crystalline fraction is very dependent on the cooling rate. Experimental images of Samples with different cooling rates can be seen in Figure 54. For a  $1^{\circ}\text{C/s}$  cooling rate, the crystallization began as very fine crystals after approximately 10s for both Samples. As the temperature of the hot side decreased, all three morphological crystals formed - faceted, columnar, and equiaxed. Some of the equiaxed crystals were transported to the hot side by fluid flow, where they dissolved when the temperature of the hot side was above the melting point.

**$1^{\circ}\text{C/s}$**

**$6^{\circ}\text{C/s}$**

**$3^{\circ}\text{C/s}$**

**$9^{\circ}\text{C/s}$**

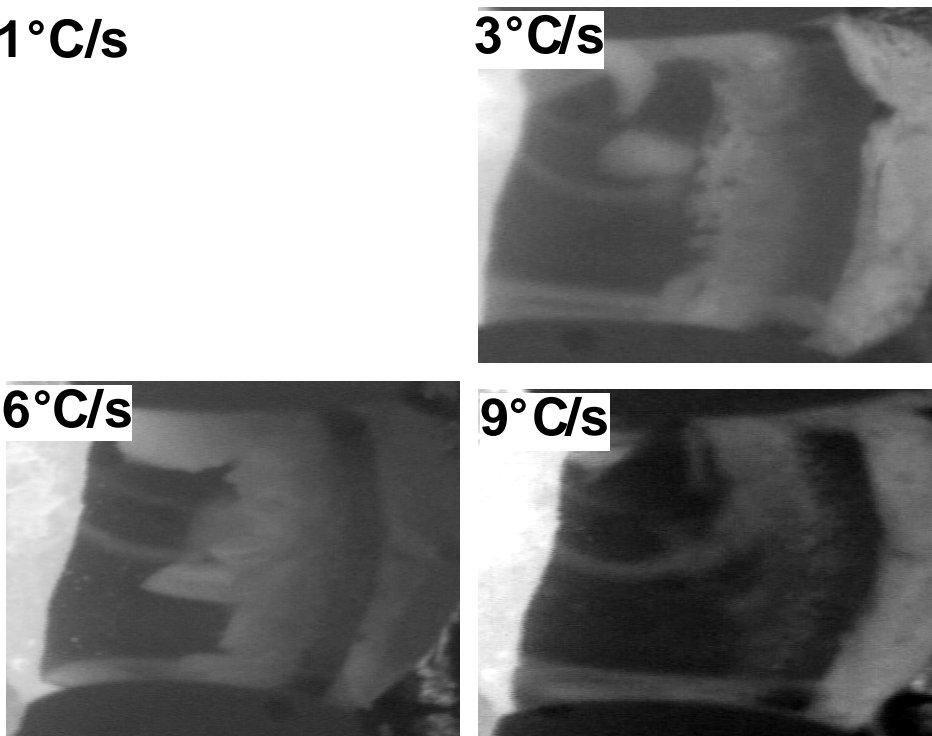


**Figure 54. Experimental Images for Different Cooling Rates of the Hot Side (Left Hand Side) taken 60s after Experiment Start. The Transparent Phase close to the Right Hand Side is Glassy, the Gray Phase is Crystalline, and the Left Side is Remaining Liquid.**

The crystalline fraction formed a dense structure, and grew towards the hot side as a front (Figure 54). As crystallization proceeded the composition of the remaining liquid changed due to rejection of solute. A liquid slag layer of at least 0.1 mm thickness remained down to 1000°C at the hot side. If the composition of the liquid layer were the same as the original slag composition, it would be fully solidified according to the TTT diagram. To ensure lubrication through the full length of the mold, the understanding of segregation during the crystallization of mold slags might indeed be a key issue when choosing the mold slag composition. With an increasing cooling rate (3°C/s and 6°C/s), not all of the equiaxed crystals dissolved at the hot side, due to a faster decrease in temperature of the hot side. The crystalline fraction appeared more fragmented and liquid/glassy pockets formed in the crystalline structure (Figure 54). With a high cooling rate (9°C/s), the crystal growth rate decreased quickly, and the crystals appeared as a small fraction of fine and faceted crystals (Figure 54).

The fraction of crystalline area, as a function of time, was measured for different cooling rates of the hot side. The results are shown in Figures 55- 57.

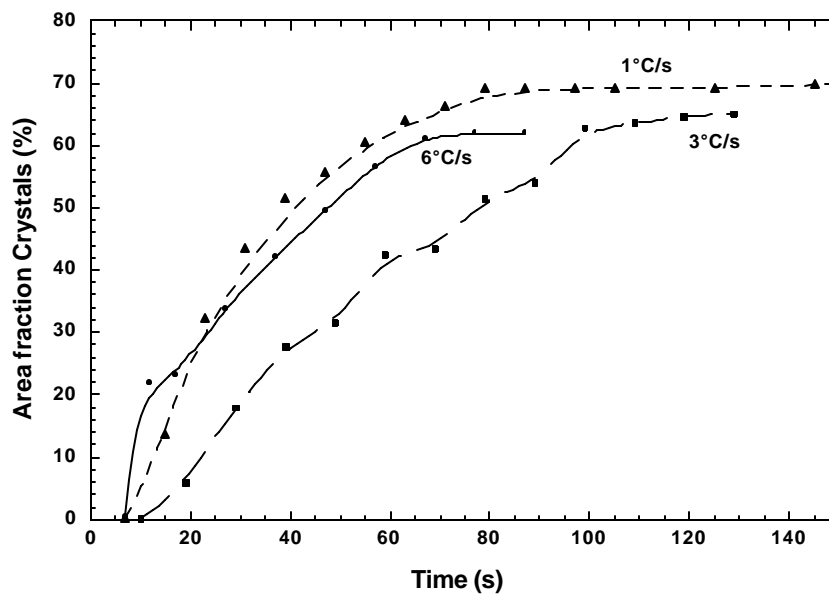


**Figure 55. Crystalline Fraction as a Function of Time for Different Cooling Rates.**

The maximum of crystalline fraction decreases with increasing cooling rate. In Figure 57, the maximum area fraction of crystal decreases from 70% to 10% when going from 1°C/s to 15°C/s cooling rate.

Thus this study has shown that by increasing the content of CaO and decreasing the content of  $\text{Al}_2\text{O}_3$  in the mold slag, the time for the beginning of crystallization was decreased. It was also found that  $\text{Na}_2\text{O}$  has a strong effect of decreasing the time for the onset of crystallization, which is in agreement with previous studies. Depending on the degree of undercooling, different crystal morphologies were observed. The amount of

crystalline fraction depends greatly on the cooling rate. Increased cooling rate drastically reduces the crystalline fraction. Larnite,  $\beta\text{-Ca}_2\text{SiO}_4$ , was precipitated at all isothermal temperatures for the experimental mold slags. The use of the DHTT for differential thermal studies is an excellent manner in which to study the solidification of mold slags as it allows one to quantify the detailed effects of a complex thermal history on the morphology and crystal structure of a solidified slag.

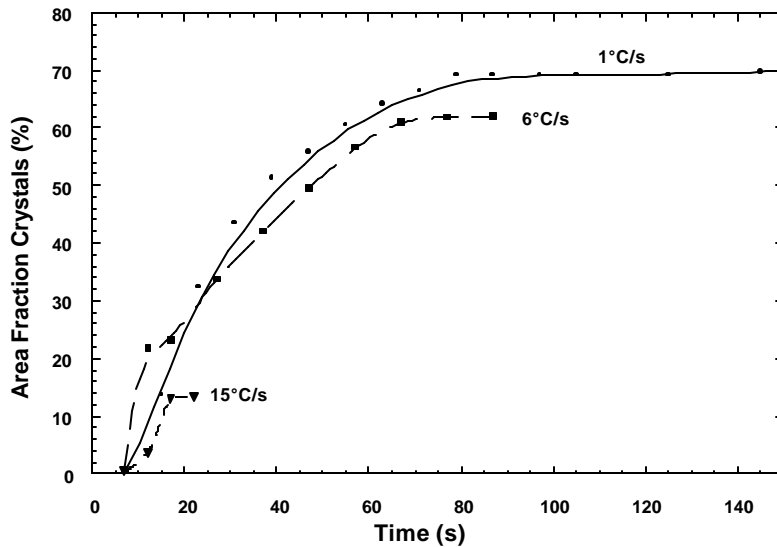


**Figure 56: Crystalline Fraction as a Function of Time for Different Cooling Rates.**

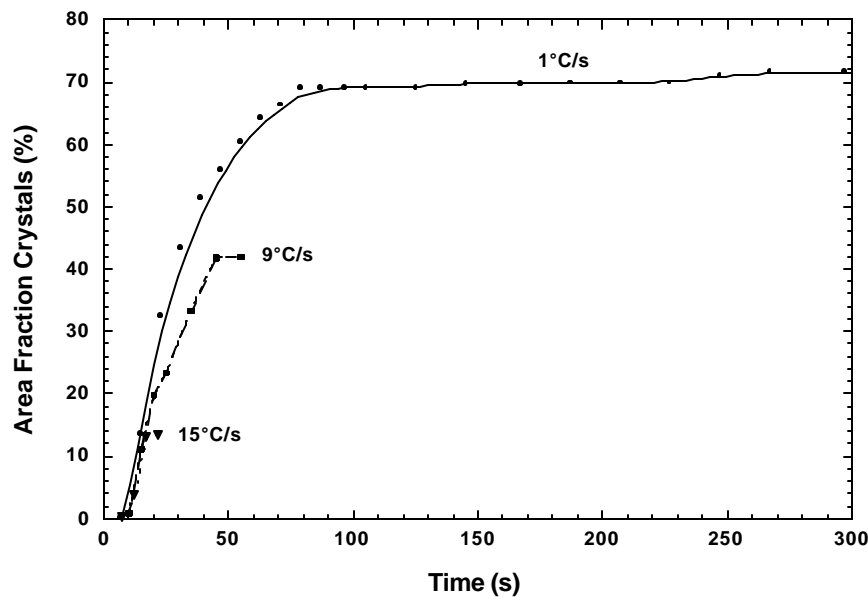


**Figure 57. Crystalline Fraction as a Function of Time for Different Cooling Rates.**

The technique is not, however, without some problems, especially when viewing slags containing high fluorine or FeO or MnO contents.

The crystallization behavior of some experimental mold slags was investigated using the double hot thermocouple technique. The compositions of the slags are shown in Table 5. The experiments involved both isothermal and continuous cooling experiments, in order to obtain TTT and CCT diagrams.

**Table 5: Industrial Mold Slag Composition**

wt%	GR-5030	STSP-816	LV 509/BC	S-A	M481
<b>CaO</b>	35.61	32.7	23.4	32.94	34.10
<b>SiO<sub>2</sub></b>	34.64	38.36	36.5	31.81	39.00
<b>Fe<sub>2</sub>O<sub>3</sub></b>	0.46	0.52	0.05	0.16	0.30
<b>K<sub>2</sub>O</b>	< 0.5	0.08	-	0.27	0.20
<b>Na<sub>2</sub>O</b>	10.23	7.75	13.13	11.35	16.80
<b>Li<sub>2</sub>O</b>	1.18	1.00			
<b>BaO</b>	0.23				
<b>Al<sub>2</sub>O<sub>3</sub></b>	6.43	4.63	6.85	2.60	3.80
<b>MgO</b>	0.5	0.33	2.67	0.18	1.30
<b>F(ion)</b>	7.00	7.79		8.84	7.4
<b>C(total)</b>	4.14	4.53		6.43	
<b>TiO<sub>2</sub></b>	<0.1	0.05			
<b>Cr<sub>2</sub>O<sub>3</sub></b>			0.08		
<b>CaF<sub>2</sub></b>			16.94		
<b>C/S</b>	1.03	0.85	0.64	1.04	0.87

The obtained TTT and CCT curves for beginning of crystallization for GR-5030, S-A, and STSP 816 are shown in Figures 58, 59 and 60, respectively.



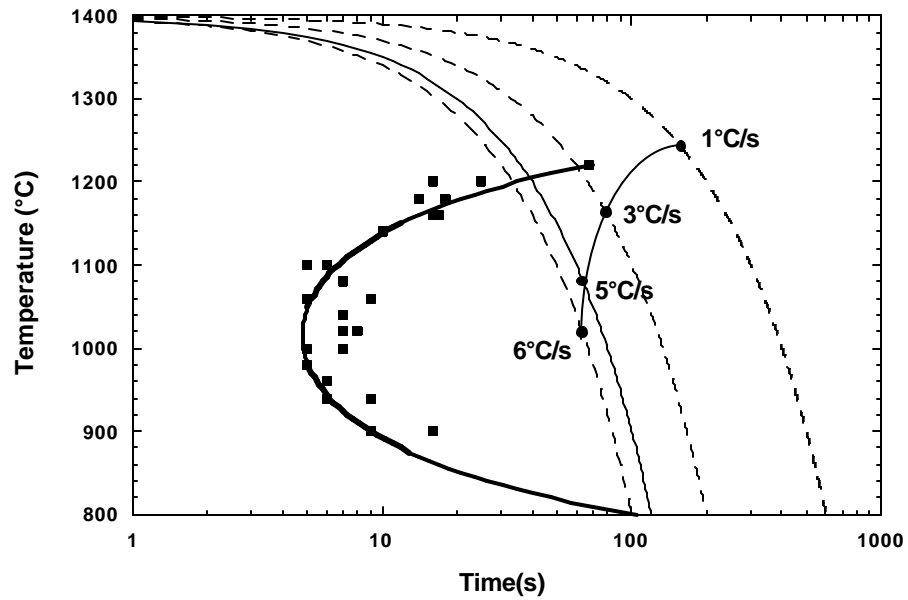


Figure 58. TTT and CCT Curve for Beginning of Crystallization for GR-5030.

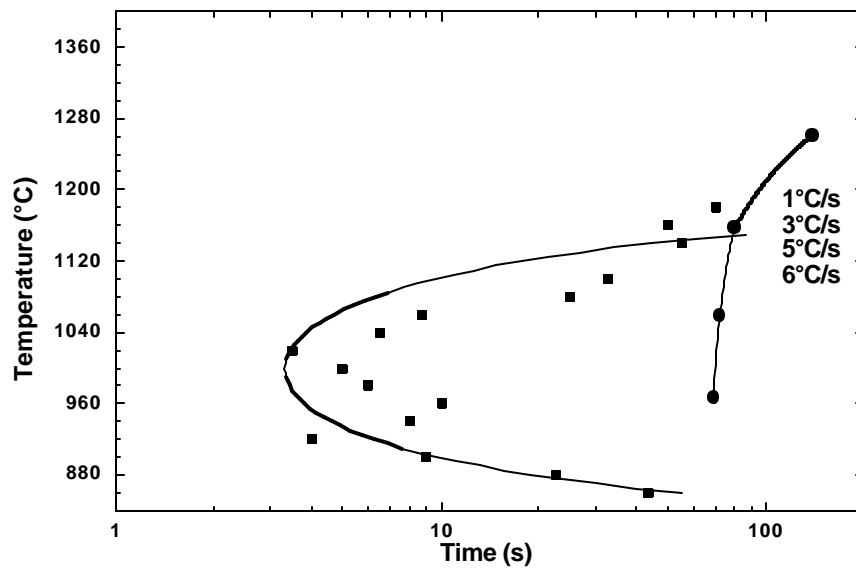
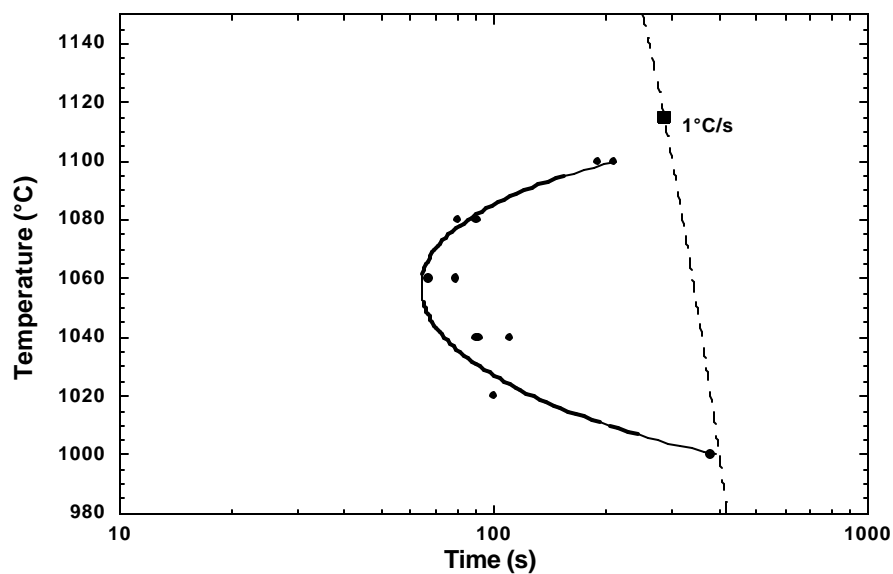


Figure 59. TTT and CCT Curve for Beginning of Crystallization for S-A.

It can be seen that the onset of crystallization occurs much faster for the isothermal experiments than for the continuous cooling experiments for GR-5030, and S-A. These two TTT curves are similar to the TTT curve obtained for Sample E3, which has almost the same basicity and contents of  $\text{Na}_2\text{O}$  and  $\text{Al}_2\text{O}_3$ . The nose position for the isothermal experiments was determined to be at  $1020^\circ\text{C}$  and 4.7s for GR-5030, and at  $1000^\circ\text{C}$  and 3.3s for S-A. The critical cooling rates for glass formation are  $45^\circ\text{C/s}$  and  $54.5^\circ\text{C/s}$  for GR-5030 and S-A, respectively. However, during continuous cooling, no visible crystallization occurred at cooling rates over  $6^\circ\text{C/s}$  for both Samples. It is obvious that the crystallization kinetics drastically change with a transient thermal field. An odd result, especially for Sample S-A is that the crystallization temperature for  $1^\circ\text{C/s}$  cooling is above the maximum crystallization temperature measured during the isothermal experiments. The reason for this is the fluorine vaporization. In the isothermal experiments, the Sample is quickly melted and held for approximately 30s at  $1400^\circ\text{C}$  before cooling to the experimental temperature. For the  $1^\circ\text{C/s}$  experiment, the Sample is also quickly melted and held 30s at  $1400^\circ\text{C}$  before the cooling starts. However, while the temperature of the isothermal Sample drops fast, the  $1^\circ\text{C/s}$  Sample spends some significant time at temperatures above the maximum crystallization temperature measured for the isothermal experiments. It is well known that the fluorine vaporization increases with increasing temperature, and therefore more fluorine escapes the  $1^\circ\text{C/s}$  Sample. Fluorides are fluxing agents, reducing the liquidus point, and so loss of fluorine will increase the crystallization temperature.



**Figure 60. TTT and CCT Curve for Beginning of Crystallization for STSP-816.**

It was observed that crystallization of GR-5030, S-A, and STSP-816 occurred at a higher temperature for experiments with a low cooling rate than that observed during the isothermal experiment. This phenomenon might be due to fluoride vaporization, which would change the composition, and subsequently the thermal region for crystallization.

The starting temperature for the experiments, before cooling, was the same for the isothermal and continuously cooled tests. At low cooling rates, the Sample spends a longer time at an elevated temperature, and would, therefore, lose more fluorine increasing the liquidus temperature of the Sample. The starting temperature for the continuously cooled experiments was decreased by 100°C for S-A, and the generated CCT curve was compared with the original CCT curve. The results are shown in Figure 61.

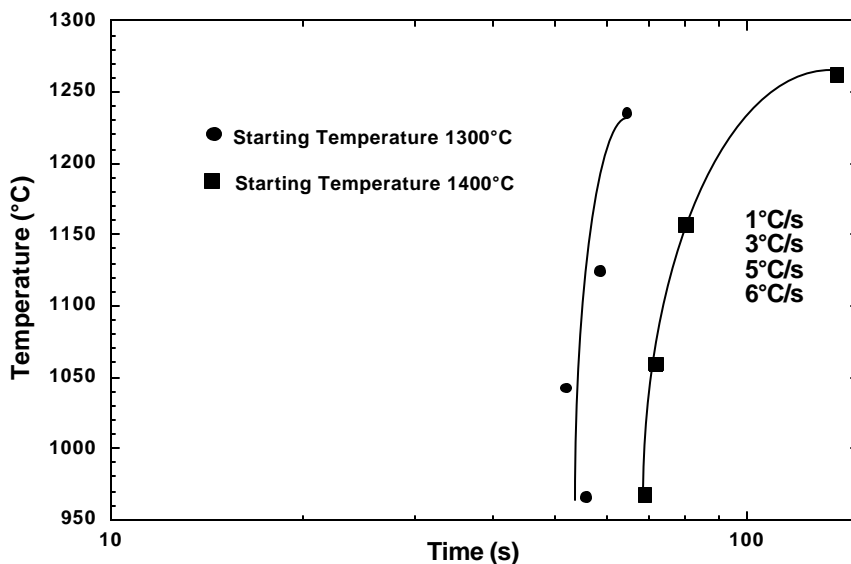


**Figure 61. The Effect of Start Temperature for the Determination of CCT Curve for S-A.**

The time for the onset of crystallization decreases naturally when the start temperature is decreased from 1400°C to 1300°C. The crystallization temperature decreased with decreasing start temperature for cooling rates of 1°C/s and 3°C/s. However, for higher cooling rates of 5°C/s and 6°C/s, the crystallization temperature was the same. It was also found that the start temperature did not affect the critical cooling rate for glass formation.

It was expected that LV 905/BC and M481 would show a similar behavior to STSP-816. M481 and STSP-816 have almost the same basicity, but M481 has twice the amount of Na<sub>2</sub>O. LV 905/BC had the lowest basicity of all the Samples, but contained the highest content of CaF<sub>2</sub>, and almost as much Na<sub>2</sub>O as M481. The results from both the isothermal experiments and the continuously cooled experiments are shown in Figures 62 and 63 for M481 and LV 905/BC, respectively.

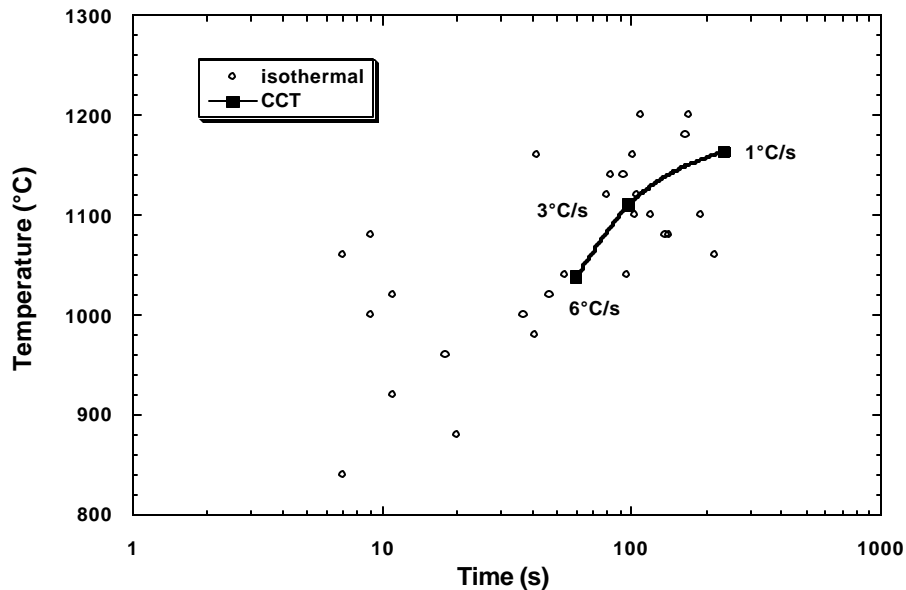


**Figure 62. Onset of Crystallization under both Isothermal and Continuously Cooled Experiments for M481.**

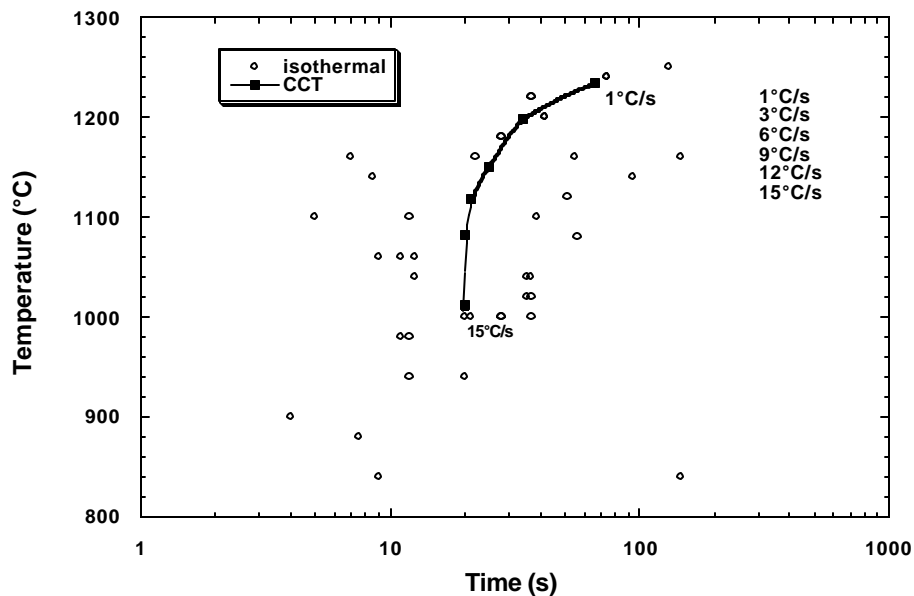


**Figure 63. Onset of Crystallization under both Isothermal and Continuously Cooled Experiments for LV 905/BC.**

The isothermal data are very scattered for both Samples, but M481 seems to exhibit a first nose between 1220°C and 1100°C. The data shown in Figures 62 are average data from results closest to each other. The determined crystallization temperatures remain

scattered for isothermal experiments even with the average data. It was first thought that the Samples were not well mixed, and that compositional differences existed between specimens. However, both M481 and LV/905BC were prefused Samples. Additional mixing of the powder had no effect in reducing the scatter in the results. The fluorine vaporization was suspected to cause the scatter and great care was taken to minimize the time at elevated temperatures. Unfortunately, the minimization of exposure time to elevated temperatures did not reduce the scatter in data.

The results from continuously cooled experiments are less scattered, and CCT curves could be obtained. In the case of M481, the critical cooling rate was found to be 6°C/s and for LV 905/BC, 15°C/s. The critical cooling rates ( $R_c$ ) for glass formation of the investigated industrial Samples have been summarized in Table 6.

**Table 6. Critical Cooling Rates for Glass Formation of Industrial Mold Slags.**

Sample	$R_c(TTT)$	$R_c(CCT)$
GR-5030	45°C/s	6°C/s
LV 905/BC	N/A	15°C/s
STSP-816	0.64°C/s	< 1°C/s
S-A	54.5°C/s	6°C/s
M481	N/A	6°C/s

### 3. Conclusions

As the demand for increased product quality and productivity continues to rise, a detailed knowledge of every aspect of the process is necessary. Slag crystallization is just one of many phenomena, affecting the final product, that occurs during the processing of steel. For a successful outcome of making a certain steel grade, the crystallization behavior of a mold slag is just as important as decarburization or desulphurization, but the fundamental understanding of slag crystallization has been limited.

In this study, slag crystallization phenomena have been studied *in situ*, allowing many details of crystallization in oxide and oxyfluoride melts to be revealed. Slag crystallization shows much resemblance with metal solidification. The precipitated crystals form in many cases columnar or equiaxed dendrites with primary, secondary and tertiary arms. The diffusion field around the dendrite tips can be described by the classical Ivantsov's solution. The structure of liquid slags differs, however, significantly from the structure of liquid metals. It is possible to undercool slags, with a significant amount of SiO<sub>2</sub>, 500°C below the melting point of the slag. The critical cooling rate for glass formation of a slag under continuous cooling conditions can range from 1°C/s to greater than 250°C/s depending on slag chemistry.

One of the most important findings in this study is the strong effect of the surroundings on the slag crystallization rate. The type of atmosphere has a decisive effect on the crystallization behavior for slag systems. It was proven that the presence of H<sub>2</sub>O (g) and not H<sub>2</sub> (g), as previously claimed, increased the extent of crystallization. Control of the

moisture content of the mold powder is an important parameter for satisfactory performance of the mold slag in continuous casting.

The slag crystallization fits in many cases, empirical relations such as the Avrami equation or the additivity principle. The use of empirical relations adds limited understanding of the crystallization mechanisms. With the advantage of *in situ* observation and the ability of easily performing experiments over a wide range of thermal conditions, the use of empirical expression to explain crystallization becomes somewhat obsolete.

Slags exhibit the same behavior as water upon solidification; the density of the solid is less than the density of the liquid. We are very fortunate that nature, in this case, works in our advantage. Had it been the other way around, slag refining would have been very difficult.

In this work the following was accomplished:

The solidification behavior of CaO-Al<sub>2</sub>O<sub>3</sub> based slags and the ternary CaO-Al<sub>2</sub>O<sub>3</sub>-MgO based slags were investigated with the double hot thermocouple technique (DHTT). Isothermal and continuous cooling experiments were employed to study these slag samples. These experiments were conducted under both dry and humid atmospheres. These slag samples were easily undercooled and the solidification behavior of CaO-Al<sub>2</sub>O<sub>3</sub> based slags was found to be a strong function of cooling rate. Then, TTT diagrams of these slag samples were created. The TTT and CCT diagrams of CaO-Al<sub>2</sub>O<sub>3</sub> based slags and TTT and CCT diagrams of ternary CaO-Al<sub>2</sub>O<sub>3</sub>-MgO based slag were generated for the first time in this work. All of the slags evaluated could form glasses at a high cooling rate and an intermediate crystalline/glass structure at moderate cooling rates.

In CaO-Al<sub>2</sub>O<sub>3</sub> based slags, the position of the TTT curve changes with the chemical composition of the slag samples and the ease of glass formation follows the trends suggested by the phase diagram. The higher the liquidus, the higher is the cooling rate necessary to form a glass. The easiest glass forming composition is the eutectic composition.

In CaO-Al<sub>2</sub>O<sub>3</sub>-MgO based slags (CaO:Al<sub>2</sub>O<sub>3</sub>≈1), the increase in MgO content also causes the position and the shape of TTT curves to change. When the MgO content increases from 0 to 3.6 % MgO, the TTT curve moves slightly upward in temperature toward lower times. After the MgO content changes from 3.6 to 7.1 % MgO, the shape of the TTT curve changes and becomes a double nose curve, where the nose at high temperature is behind the nose at low temperature. For 9 % MgO slag sample, the shape of the TTT curve is also double nose and the position of TTT curve moves slightly in front of the TTT curve of the 7.1 % MgO slag sample. Thus, the ability of a given slag to form a glass follows the liquidus surface of the phase diagram. Similar results were found when silica and boron were added.

Normally, critical cooling rate is used as the parameter for a determination of the crystallization tendency or of glass formation. A high critical cooling rate means the high crystallization tendency. The critical cooling rate of these slag samples was estimated from the position of the nose of TTT curves and this critical cooling rate was compared to

the critical cooling rate obtained from CCT curves. It was found that the critical cooling rate from TTT curve is always more than the critical cooling rate from CCT curve as expected. In CaO-Al<sub>2</sub>O<sub>3</sub> based slags, the eutectic composition gives the lowest critical cooling rate due to the lowest liquidus temperature from eutectic composition. In CaO-Al<sub>2</sub>O<sub>3</sub>-MgO based slags, the critical cooling rate increases with MgO content because the high MgO content lead to the high liquidus temperature.

In this work, the effect of dissolved water on the solidification behavior of these slags was also studied. In a eutectic CaO-Al<sub>2</sub>O<sub>3</sub> slag sample, dissolved water in the sample changes the position of the TTT curve by moving the TTT to higher temperature and lower times, thus to higher critical cooling rate. The dissolved water content also enhances the growth velocity of eutectic CaO-Al<sub>2</sub>O<sub>3</sub> slag sample. Thus it can be concluded that dissolved water enhanced the crystallization tendency of this slag. It was also found that the crystalline phase that formed during cooling in both the dry and humid conditions is the mixture between 3CaO.Al<sub>2</sub>O<sub>3</sub> and CaO.Al<sub>2</sub>O<sub>3</sub> phases.

In CaO-Al<sub>2</sub>O<sub>3</sub>-MgO slag samples, in general there was little effect of water vapor in solidification behavior compared to CaO-Al<sub>2</sub>O<sub>3</sub> based slags. It was found that dissolved water hinders the crystallization behavior of 3CaO.Al<sub>2</sub>O<sub>3</sub>+3CaO.2Al<sub>2</sub>O<sub>3</sub>.MgO, which formed at high temperature and had no effect on crystallization of 3CaO.Al<sub>2</sub>O<sub>3</sub>+MgO.Al<sub>2</sub>O<sub>3</sub>, which formed at low temperature. The effect of dissolved of water on the crystallization of CaO-Al<sub>2</sub>O<sub>3</sub>-MgO based slags is not as prominent as in the eutectic CaO-Al<sub>2</sub>O<sub>3</sub> slag. Thus, the addition of MgO to CaO-Al<sub>2</sub>O<sub>3</sub> slags was seen to minimize or eliminate the effect of humidity on the solidification of CaO-Al<sub>2</sub>O<sub>3</sub> based slags. This is also a novel and major finding of this work.

The growth velocity of CaO-Al<sub>2</sub>O<sub>3</sub> based slags and of ternary CaO-Al<sub>2</sub>O<sub>3</sub>-MgO based slags were measured for the first time. In CaO-Al<sub>2</sub>O<sub>3</sub> based slags, the growth velocity was in the range between 5 to 350 μm/sec. depending on temperature and composition of the slag samples. At a given isothermal temperature, the eutectic CaO-Al<sub>2</sub>O<sub>3</sub> slag sample gave the slowest growth velocity. In all slag samples, increased isothermal temperature enhanced diffusion rate and resulted in a higher growth velocity. Dissolved water in the eutectic CaO-Al<sub>2</sub>O<sub>3</sub> slag sample decreased the viscosity of the slags by breaking tetrahedral network in the structure of liquid slags due to segregation during solidification and this resulted a in higher local growth velocity. In CaO-Al<sub>2</sub>O<sub>3</sub>-MgO based slags, for isothermal temperatures below 1200°C, the growth velocity of all CaO-Al<sub>2</sub>O<sub>3</sub>-MgO slag samples increased with increasing isothermal temperature and MgO content. For isothermal temperatures above 1200° C, the growth velocity decreased. This occurred because the growth velocity was retarded by the formation of the new phase from the second nose of the TTT curve. Dissolved water enhanced the growth velocity when isothermal temperature was lower than 1170°C and hindered the growth velocity when isothermal temperature is higher than 1170°C.

Uhlmann's method was used to estimate the solid-liquid interfacial energy of CaO-Al<sub>2</sub>O<sub>3</sub> based slag for the temperature between 1100°-1250°C. The results are shown in the following equations:

by assuming heterogeneous nucleation (40° contact angle)

$$g_{sl}(J/m^2) = 1.1893 - 0.0007 \cdot T(C)$$

Dissolved water in CaO-Al<sub>2</sub>O<sub>3</sub> based slag also increases the solid-liquid interfacial energy. And this work allows a prediction of the solid-liquid interfacial energy in presence of water:

$$g_{sl}(J/m^2) = 2.1473 - 0.0012 \bullet T(C)$$

It appears that water vapor affects solidification behavior in 2 ways: (1) It increases diffusion rate in the liquid ahead of growing interface due to segregation, and (2) It changes the solid-liquid interfacial energy of the precipitating solid. Both of these effects result in a significant change to the TTT curve. However, this also leads to our ability to predict TTT and CCT curves from knowledge of diffusivity and thermodynamics.

A significant amount of work was also carried out to determine the solidification behavior of actual mold slags with similar results to those already discussed; however, high fluorine contents in a number of fluxes made the results less clear.

This project has lead to the further development of a new tool for measuring slag solidification under a wide variety of thermal conditions and also to an improved understanding of solidification behavior in that most ubiquitous of steelmaking materials – a slag. The true nature of solidification of slags has been revealed and new scientifically based criteria have been developed for understanding slag behavior: the TTT and CCT curves, the critical cooling rate for glass formation, the effect of cooling rate on solidification morphology. Thus, both deliverables of the project have been satisfied.

This work is fully documented in the thesis work of the three students who contributed to the project.

Carl Orrling: “Crystallization Phenomenon in Slags”, Carnegie Mellon University, Doctoral Thesis, 2000

This is the pioneering work on development of the technique and application to industrial practice.

Heather Creely: “Solidification of Slags”, Masters Thesis, Carnegie Mellon University, 2002

Which covers further work on environmental aspects of Solidification  
Kritstada Prapakorn: “ The Solidification Behavior of Calcium Aluminate Based Slags”, Carnegie Mellon University, 2003

This is a very detailed study of fundamental binary and ternary systems.

All of these theses are available to anyone who wishes a more detailed discussion of the work.



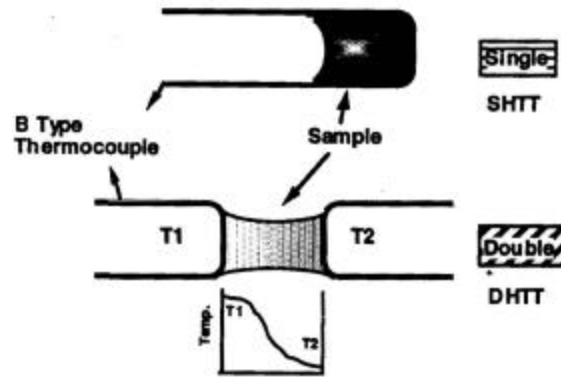
## Appendix 1: Experimental Technique

### 1.1 Experimental Equipment

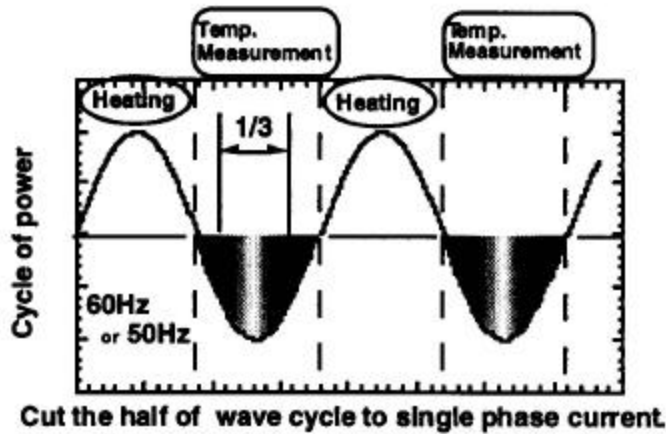
#### 1.1.1 Double hot thermocouple technique (DHTT)

In this work, the double hot thermocouple technique (DHTT) was used as the main experimental apparatus. This technique enables crystallization phenomena in transparent liquid slags to be observed “*in situ*” due to the transparency of slag sample. The samples from the DHTT can be further analyzed with other techniques, such as scanning electron microscope (SEM) and x-ray diffraction.

The hot thermocouple method was invented by Ordway and Welch. Ishii and Kashiwaya first developed the DHTT by improving the single hot thermocouple technique (SHTT). The hot thermocouple method is controlled by a hot thermocouple driver, which permits temperature measurement and simultaneous heating. In this method, the slag sample is heated and melted directly on the tip of one thermocouple (as in SHTT) or between two similarly figured two thermocouples (as in DHTT). The difference between DHTT and SHTT is shown in Figure 1.1.



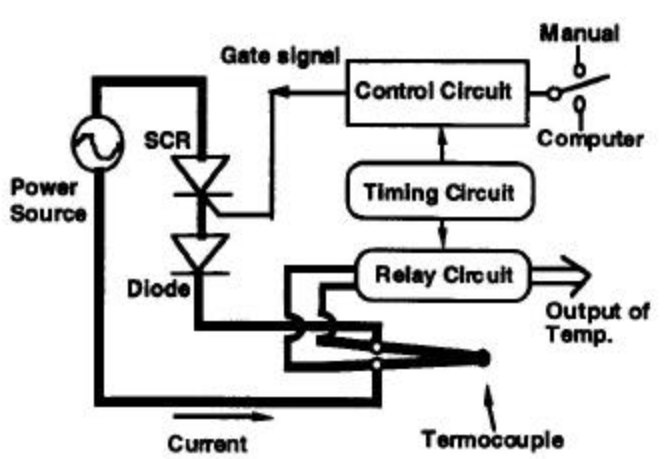
**Figure 1.1 Illustration of Double Hot Thermocouple (DHTT) and Single Hot Thermocouple (SHTT).**



**Figure 1.2 Principle of Hot Thermocouple Driver.**

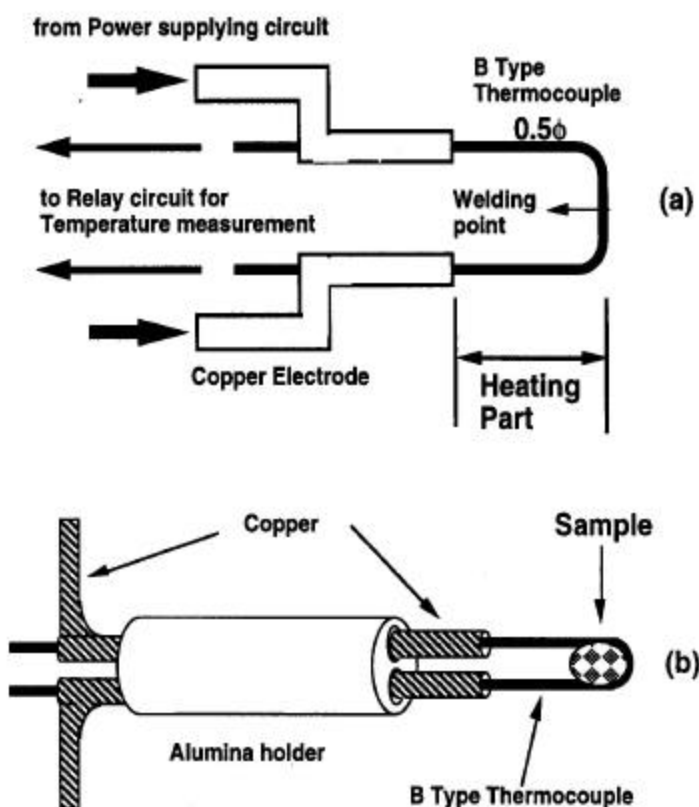
The principle of the hot thermocouple driver is shown in Figure 1.2. The cycle of electrical current (60 Hz) is rectified into a half-wave by silicon controlled rectifier (SCR). The total cycle occurs every 1/60 second, so that the heating cycle (first half of wave) occurs for a maximum length of 1/120 sec. and is then followed by a similar period when there is no current input. During second cycle, the temperature of thermocouple is measured by using a relay circuit, which is turned on only for 33% of 1/120 sec. in order to minimize the heating noise.

Figure 1.3 shows a schematic of the circuit for hot thermocouple driver. The main circuit is the power supply circuit having a SCR and a diode. To control the SCR, the gate signal is supplied from the power control circuit (or temperature control circuit) which is operated by means of computer or potentiometer (manual). Because the temperature will change with the length of thermocouple wire and the amount of the sample, the temperature is not always constant when the same D.C. voltage is supplied to the control circuit. The output of electromotive force from thermocouple is connected to the relay circuit, which is turned on only during one third of the no heating (temperature measurement) period to reduce noise.



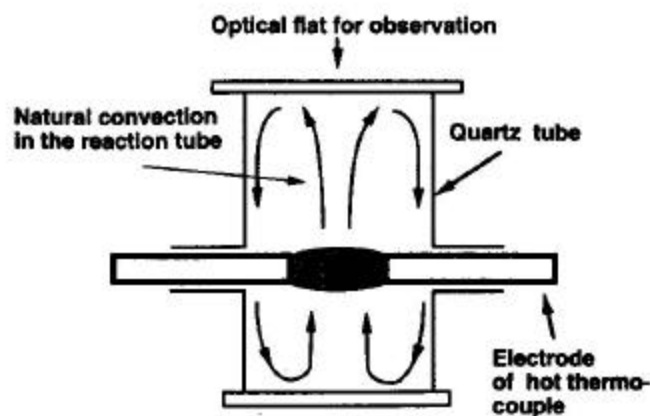
**Figure 1.3 Circuit Diagram of the Hot Thermocouple Driver.**

Figure 1.4 shows the schematic of the electrode, which is used to hold a hot thermocouple. The two sides of B-type thermocouple (Pt-30%Rh for positive side and Pt-6%Rh) are welded together at the ends to form a square loop. The welding point, which is the point for the temperature measurement, is located in the middle of the loop. The most important experimental technique that must be mastered is to weld the thermocouple without a bead and to make it same diameter. A wider or smaller diameter of hot thermocouple causes non-uniform heat generation. The maximum achievable temperature varies with the length of thermocouple wire connected to the copper electrodes. The achievable cooling rate is a function of the length of thermocouple wire and the heat transfer mechanism that controls heat loss from the sample. Tight contact between thermocouple and copper electrode is important for noiseless measurement.



**Figure 1.4 Schematic of (a) Electrode Junction and (b) Electrode Assembly**

The two thermocouples, which hold the sample, are placed in the reaction chamber (as shown in Figure 1.5). Figure 1.5 also shows the natural convection of gas in the reaction tube. Kashiwaya indicated that the sample temperature increased under microgravity when natural convection was minimized, even though the power to the hot thermocouple was constant. In order to obtain a stable temperature, natural convection must be stabilized. It was also found that the heat loss increased with the gas stream. Thus, a supplemental heater was employed to minimize the heat loss from the surface of the sample to the ambient gas. The supplemental heater was made of platinum wire and was located under the sample.



**Figure 1.5 Schematic of Convection Patterns in the Reaction Chamber**

Figure 1.6 shows details of the experimental apparatus that is attached to the DHTT. The additional apparatus includes an aluminum reaction chamber with quartz window, hot thermocouple drivers for each thermocouple, a data acquisition board, a computer, an observation system consisting of a microscope, a 3CCD camera, a timer, a character generator and a VCR. From this figure, the sample was hung between two tips of B-type thermocouple in the reaction chamber under microscope.

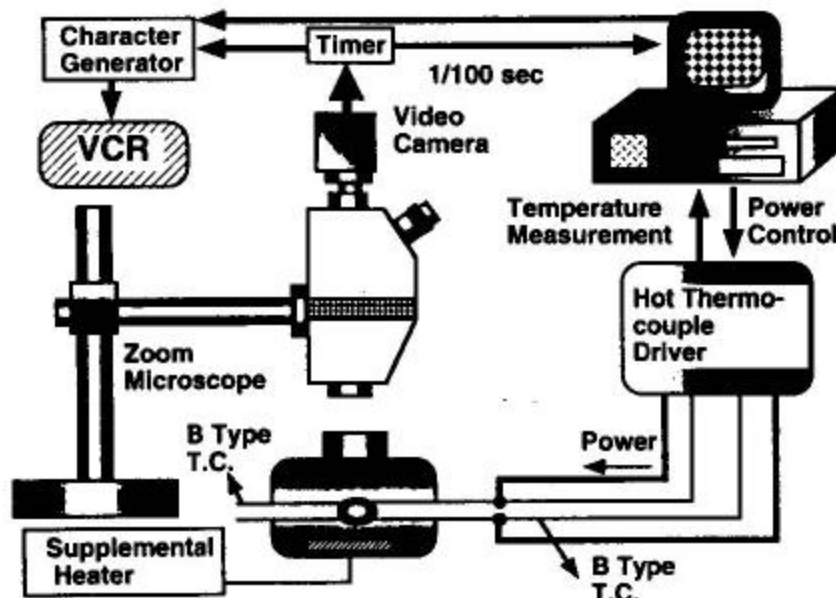


**Figure 1.6 Schematic of Experimental Apparatus**

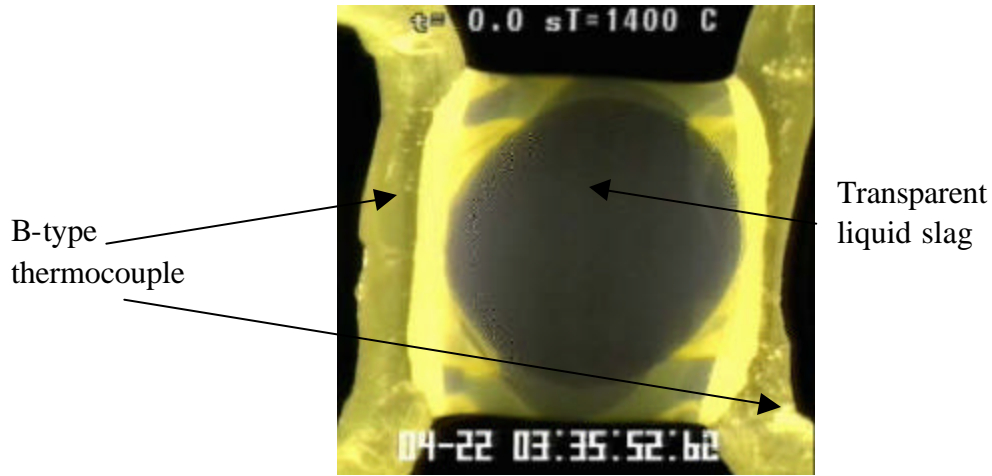


**Figure 1.7 Image of Transparent Liquid Slag Sample in DHTT**

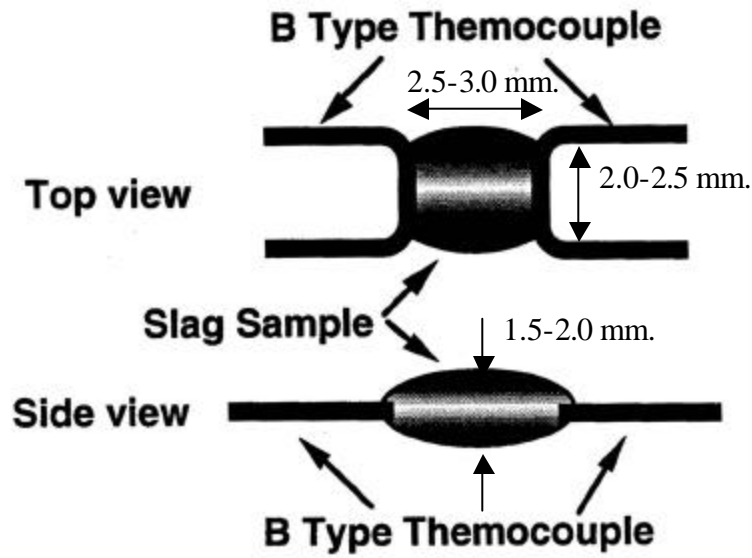


**Figure 1.8 Illustration of Shape and Size of Slag Sample in DHTT**

Figure 1.7 shows an image of the transparent liquid slag sample in the DHTT. Figure 1.8 shows the shape and size of the sample. The computer controls the thermocouple driver through a two-channel D/A (digital to analog) interface that enable individual heating and cooling control of the thermocouples. The temperature from hot thermocouples is measured via an A/D (analog to digital) interface to the computer. The computer uses a Proportional and Integral (PI) control program that allows precise temperature control. The mathematical formula for the PI control is expressed as follows:

$$Power = \max(P_{out}) - C_1 \cdot \left( C_2 \cdot \int \Delta T dt - \Delta T \right) \quad (1-1)$$

Where,

$\Delta T$  = Preset temperature-Actual temperature

$P_{out}$  is power output.

$C_1$  and  $C_2$  are constant.

In the case of continuous cooling experiment, the preset temperature is defined as:

Preset temperature = Initial temperature – time \* cooling rate

The control program manages the thermal history of the sample where cooling rate or temperature varies with time, such as in isothermal or continuous cooling. The PI control option eliminated the temperature difference between the preset temperature and actual temperature by adjusting the control power until the temperature difference becomes zero.

After recording the image of the sample, the time and the temperature are added onto the image by timer and character generator. Finally, the image is recorded for further analysis.

## 1.2 Experimental method

In order to measure crystallization tendency, two typical methods were employed.

### 1. Continuous cooling experiments (as shown in Figure 1.9)

In this method, the sample was heated to 1600 °C, above the equilibrium melting point. At this temperature, the sample became transparent. Next, the sample was held at this temperature for 5 minute to allow homogeneity of the sample. After that, the sample was cooled to 900 °C. The cooling rate was varied from 0.1° to 50 °C/minute. The CCT (continuous cooling transformation) curve was created from this experiment. In this method, its cooling rate was fixed but degree of undercooling varied.

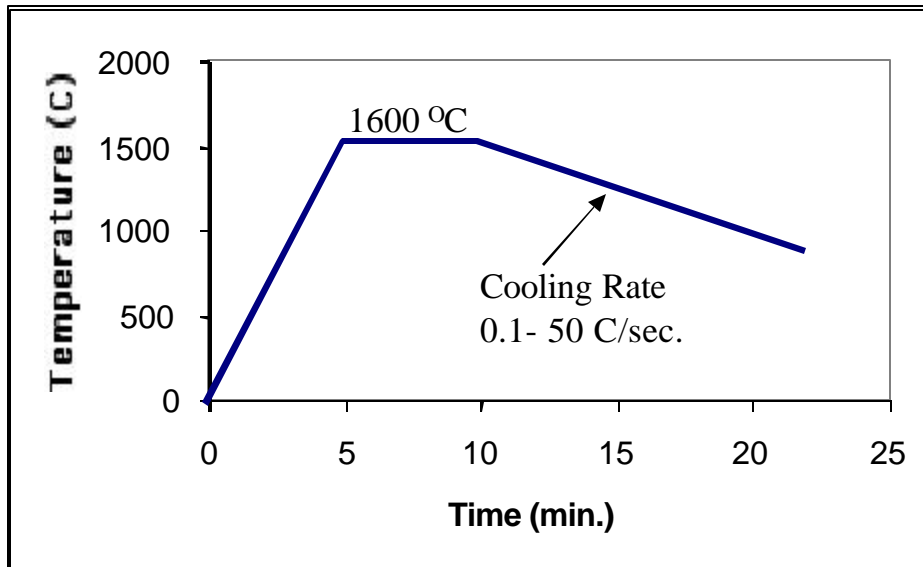


**Figure 1.9 Temperature History of the Sample from Continuous Cooling Experiment.**

2. Isothermal experiment ( as shown in Figure 1.10)

In this method, the sample was heated to 1600 °C and held for 5 minutes. Then, the sample was cooled down to the isothermal temperature within at a cooling rate of 200 C/sec. The isothermal temperature varied from 960° to 1260 °C. The result from this experiment can be used for creating the TTT (Time-Temperature Transformation) curve. In this method, degree of undercooling was fixed.

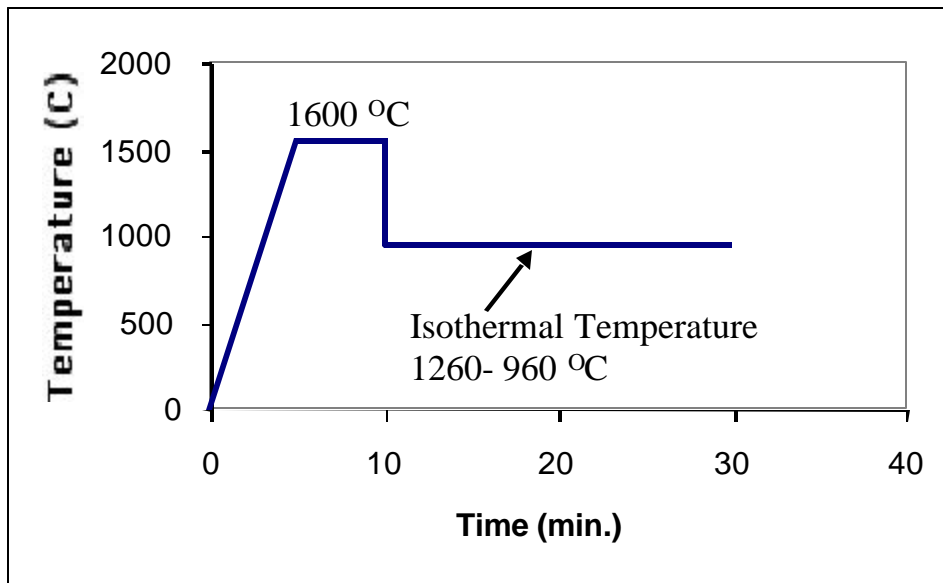


**Figure 1.10 Temperature History of the Sample from Isothermal Experiment**

In order to study the effect of water vapor on crystallization, these two methods were conducted in 2 different atmospheres: UHP-Ar and UHP-Ar +water vapor.

The UHP-Ar +water vapor mixture was prepared by passing UHP-Ar gas 150 ml/min through a water column, where its temperature has fixed and controlled by a condenser. The experimental partial pressure of water vapor used in this study were 0.012, 0.054 and 0.196 atm, which are equivalent to full humidity at 10°, 35° and 60 °C, respectively.

### 1.3 Sample

In this work, the slag samples chosen for the study had composition near the eutectic point and were produced by mechanically mixing high purity grade reagents, such as 99.99%CaO, 99.9%Al<sub>2</sub>O<sub>3</sub> and 99.9%MgO together. The mixture was then melted in graphite crucibles with induction furnace at temperature above 1700 °C. Then, the molten mixture was poured on the chill mold and solidified. The samples were then ground and decarburized at 600 °C in a muffle furnace. Finally, chemical analysis was done to check the composition of the sample.